Malaysian Journal of Catalysis
http://mjcat.utm.my/
MJCat
Research Article

Fabrication and characterization of $(Cr_2O_3)_6$ $(CdO)_4$ nanoparticles produced utilizing calcination temperature route

Naif Mohammed Al-Hada[1,2*], Rafiziana Md. Kasmani[2*], Abbas M. Al-Ghaili[3*], Hussein Baqiah[1], Muneer Aziz Saleh[4], Hairoladenan Kasim[5], M. N. Azlan[6]

[1]*Shandong Key Laboratory of Biophysics, Institute of Biophysics, Dezhou University, Dezhou 253023, China*
[2]*School of Chemical and Energy Engineering, Universiti Teknologi Malaysia, 81310 Skudai, Johor Bahru, Johor, Malaysia*
[3]*Institute of Informatics and Computing in Energy (IICE), Universiti Tenaga Nasional (UNITEN), 43000 Kajang, Selangor, Malaysia*
[3] *Office of Radiation Protection, Environmental Public Health, Washington State Department of Health*
[5]*College of Computing & Informatics (CCI), Universiti Tenaga Nasional (UNITEN), 43000 Kajang, Selangor, Malaysia*
[6]*Physics Department, Faculty of Science and Mathematics, University Pendidikan Sultan Idris, Tanjong Malim 35900, Malaysia*

**Corresponding Author: naifalhada@yahoo.com; rafiziana@utm.my;abbasghaili@yahoo.com*

Article history :
Received 1 October 2021
Accepted 30 January 2022

ABSTRACT

A unique thermal calcination temperature was used to produce $(Cr_2O_3)_{0.6}$ $(CdO)_{0.4}$ nanoparticles. X-ray diffraction (XRD), energy-dispersive X-ray spectroscopy (EDX), and field emission scanning microscopy were used to characterize the structural, morphological, and elemental composition aspects of the generated nanoparticles (FESEM). The XRD analysis demonstrated that the crystalline size has been increased after calcination. The crystalline size rose with increasing calcination temperature, and the mean grain size investigated by FESEM micrographs revealed a matching growing tendency. The existence of Cr, Cd, and O in these new compounds has been confirmed by EDX studies.

Keywords: Heat treatment; Polyvinylpyrrolidone; $(Cr_2O_3)_{0.6}$ $(CdO)_{0.4}$ nanoparticles

| eISSN 0128-2581 |

1. INTRODUCTION

Recently, the promising characteristics of semiconductor nanostructured materials have been exploited by many applications, where this has increased research's interests [1-3]. One of the most used applications is the hexagonal chromium oxide (Cr_2O_3) and cubic cadmium oxide (CdO), n-type II–VI semiconductors [4, 5]. Given that both materials have shown their capacity in gas sensing, and its mixed form i.e., Cr_2O_3-CdO might be considered as a useful material in applications such as for the photovoltaic industry [6]. Another property of mixed Cr_2O_3 and CdO might also display complementary characteristics; for example: display multiple band gaps from both oxide semiconductors that may possess significant properties from individual semiconductor components [7, 8]. However, this study is not common practise as it tries to develop a product that can fit for industrial uses, focusing on simple handling and particle sizes of varying sizes. Smaller sizes can be employed for many uses, whereas larger sizes can be used for energy applications. Other advantages include reduced cost, good quality, high flexibility, powdered form, and an effective band gap. Notably, the current approach does not necessitate the use of any extra chemical reagents. This research focuses on a unique technique for manufacturing a $(Cr_2O_3)_{0.6}$ $(CdO)_{0.4}$ nanosize and the effect of temperature [9-25].

This study describes a simple calcination temperature process to produce $(Cr_2O_3)_6$ $(CdO)_4$ nanoparticles. An overview related to producing pure nanoparticles is provided. Pure nanoparticle production is a solution containing nitrate metallic ions and PVP capping agent followed by calcination at a required temperature before undergoing structural, morphological, and optical characteristics investigation.

2. EXPERIMENTS

2.1 Materials

Chromium nitrate $Cr(NO_3)_3{\cdot}6H_2O$ and cadmium nitrate $Cd(NO_3)_2.4H_2O$ metallic salts were employed as metal precursors, polyvinyl pyrrolidone (PVP) was used as a capping agent for facilitating the dispersion of nanoparticles, and deionized water was used as a solvent. $Cr(NO_3)_3{\cdot}6H_2O$ (99%), $Cd(NO_3)_2.4H_2O$ (99%) and PVP (MW= 58,000) were procured from Sigma-Aldrich.

2.2 Method

Following the dissolution of 0.6 mmol of $Cr(NO_3)_3{\cdot}6H_2O$, 0.4mmol of $Cd(NO_3)_2.4H_2O$, and 2% PVP have been added completely to form a homogeneous solution. The resulting solution has been poured into a Petri dish and dried at a temperature of 363K for 24 h producing thereby a yellow-colored dried gel which was crushed into powder and calcined at temperatures 773, 873, 973, and 1073K. for 3 h. To determine the structural, morphological, elemental composition, and optical properties of the $(Cr_2O_3)_{0.6}$ $(CdO)_{0.4}$ nanoparticles, various analytical instruments were employed. This included powder X-ray diffraction (XRD), field emission scanning electron microscopy (FESEM), and energy-dispersive X-ray spectroscopy (EDX).

3. RESULTS AND DISCUSSION

Fig. 1 displays the XRD patterns for the samples calcined at 773, 873, 973, and 1073 K. The reflections observed for the synthesized powder confirm the existence of the hexagonal phase of Cr_2O_3 a nd cubic phase of CdO semiconductor nanoparticles. A mixture of hexagonal Cr_2O_3 semiconductor nanoparticles and cubic phase CdO semiconductor nanoparticles was displayed by the synthesized $(Cr_2O_3)_{0.6}$ $(CdO)_{0.4}$ nanoparticles. The position of the Bragg's lines of the Cr_2O_3 nanoparticles with reference to JCPDS Card 38-1479 [22], the presence of multiple diffraction peaks of (012), (104), (110) (211), and (030) in the diffraction patterns suggests that the Cr_2O_3 sample displays a characteristic hexagonal structure. Similarly, the position of Bragg's lines of CdO nanoparticles was used to determine the interplanar spacing (d), which in turn used to index the diffraction peaks. The existence of multiple diffraction peaks of (200), (220), (311), and (222) in the diffraction patterns suggests that the CdO samples have a typical face centered cubic (fcc) structure referring to the PDF Card no. 005- 0640 data [26].

The full width of the half-maximum peak broadening of the peak of the XRD patterns was employed to calculate the average crystal size, using the Scherer formula:

$$D=0.9\lambda/\beta\cos\theta \quad (1)$$

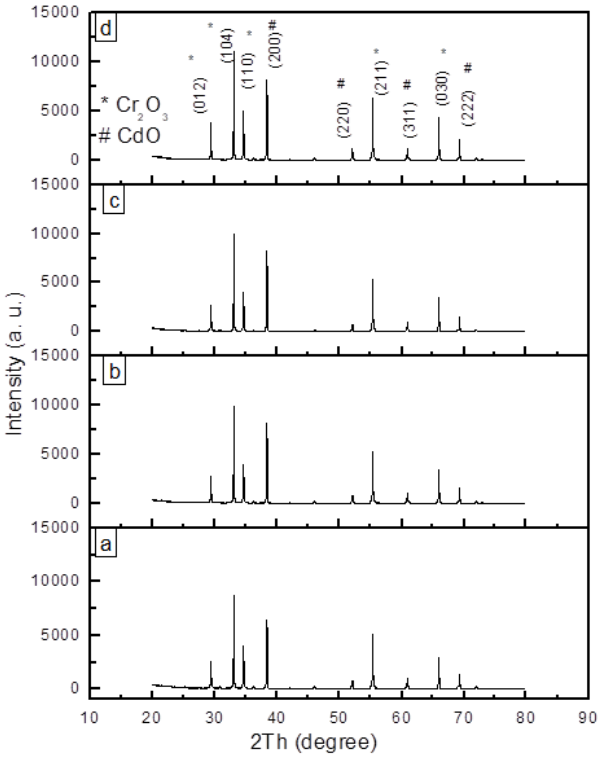

Fig. 1. XRD patterns of binary $(Cr_2O_3)_{0.6}$ $(CdO)_{0.4}$ nanoparticles prepared at various calcination temperatures: (a) 773, (b) 873, (c) 973, (d) 1073K.

Where D is the crystalline size (nm), β is the entire width of the diffraction line at half of the maximum intensity measured in radians, λ is the X-ray wavelength of Cu Kα = 0.154 nm and θ is the Bragg's angle [27]. The results displayed that the increases in crystal sizes were determined using the Scherer formula at calcination temperatures ranging from 773 -1073K as shown in Table 1. As the calcination temperature increased, a corresponding increase in the crystal size w, which is ascribed to the enlargement of grain size [28]. It is concluded from Fig. 1 (a-d) that sharper and narrower diffraction peaks with increased intensities result when the calcination temperature is raised pointing to a significant enhancement in the crystallinity.

Table 1. The crystalline size of the sample's nanoparticles calcined at various temperatures.

Calcination temperature (K)	Crystal size, D_{XRD} (nm)
773	59
873	71
973	85
1073	92

Field emission scanning electron microscopy (FESEM) in the range of 773-1073K has been used to study the surface morphology of the sample nanoparticles. Micrographs of $(Cr_2O_3)_{0.6}$ $(CdO)_{0.4}$ nanoparticles, at various calcination temperatures (773, 873, 973, and 1073 K), are displayed in Fig. 2. The Cr_2O_3 and CdO compounds are seen as homogenous. At low temperatures (Fig. 2 (a-b)), the grain size of the sample is small and virtually rod in shape with some regularities. In Fig. 2 (c-d) the grain size of sample increase and overlap (fuse together to form larger particle sizes by melting their surfaces) with increasing calcination temperature. As that the calcination temperature increased, the particles increased in size individually, resulting in a more even distribution and consistency throughout the sample (Figure 4c and Figure 4d). In order to calculate the average grain size of the sample, Image J software was used to measure the grain size of around 70 grains in a FESEM image. At temperatures of 773, 873, 973, and 1073 K, the average grain sizes are 1.84, 2.10, 2.30, and 2.55 microns, respectively.

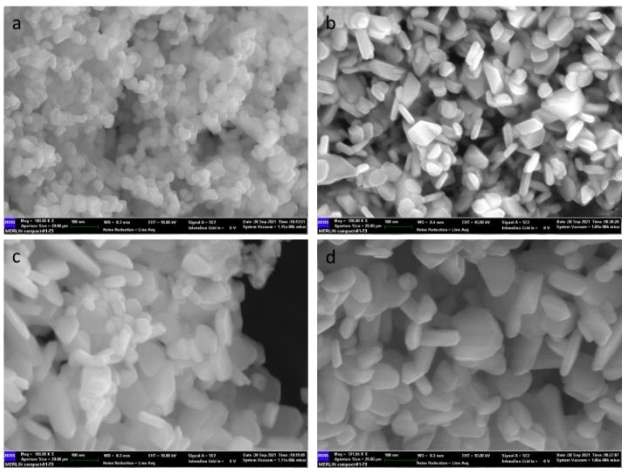

Fig. 2. FESEM images of $(Cr_2O_3)_{0.6}$ $(CdO)_{0.4}$ nanoparticles prepared at various calcination temperatures: (a) 773 (b) 873, (c) 973 and (d) 1073 K.

The EDX spectra and atomic composition of $(Cr_2O_3)_{0.6}$ $(CdO)_{0.4}$ nanoparticles formed at 873K by the calcination route are explained in Fig. 3. The fabrication of $(Cr_2O_3)_{0.6}$ $(CdO)_{0.4}$ nanoparticles has been certified by the corresponding peaks of Cr, Cd, and O produced in the sputtered sample. A 6:4 ratio of Cr to Cd precursors, correlating with their composition in the chemical formula $(Cr_2O_3)_{0.6}$ $(CdO)_{0.4}$ nanoparticles, was determined by the atomic composition (%) ratios of [Cr:O] and [Cd:O], shown to be [28: 32] % and [19: 21] % respectively. The sputtering process applied during the preparation of the sample for EDX analysis generated the peaks of Pt as seen in the spectrum. The success of the calcination employed in this work has been validated by the lack of element loss seen during the fabrication process, and the fabrication of $(Cr_2O_3)_{0.6}$ $(CdO)_{0.4}$nanoparticles as confirmed by the EDX spectrum data.

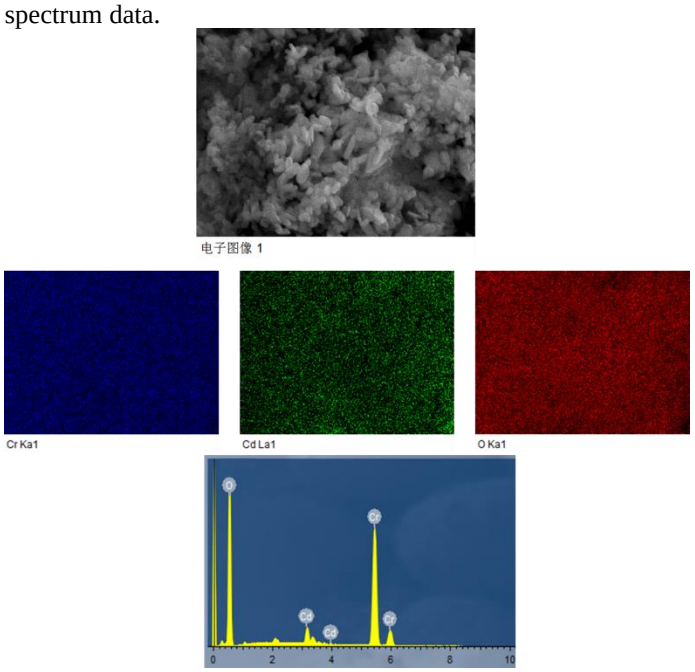

Fig. 3. Shows the EDX spectrum of the $(Cr2O3)_{0.4}(CdO)_{0.6}$ nanoparticles calcined at 873 K.

4. CONCLUSION

As proven by XRD examinations of $(Cr_2O_3)_{0.}6$ $(CdO)_{0.4}$ nanoparticles produced by the novel calcination approach, the synthesis of $(Cr_2O_3)_{0.}6$ $(CdO)_{0.4}$ nanoparticles with hexagonal and face-cantered cubic structures, respectively, was achieved at all calcination temperatures investigated. The size of the crystal was demonstrated to increase with higher calcination temperatures, as demostrated by the crystal diameters, increasing from 59 nm at 773K to 92 nm at 1073K, respectively. Further, the EDX studies shown that the peaks of Cr and Cd, an atomic composition consisting primarily of chromium was found and it was in agreement with the quantities of Cr and Cd used in the initial materials. The lack of element loss seen during the synthesis process, as well as the successful creation of $(Cr_2O_3)_{0.}6$ $(CdO)_{0.4}$ nanoparticles, demonstrated the efficiency of the thermal treatment method used in this study.

ACKNOWLEDGEMENTS

This work was supported in part by the Research Foundation for Advanced Talents of Dezhou University, in part by Universiti Teknologi Malaysia (UTM), Fellow Research Grant, Q.J130000.21A6.00P19 and MOHE- FRGS grant (R.J130000.7851.5F392).

REFERENCES

[1] L. Zhu, M. Gao, C. K. N. Peh, and G. W. Ho, Materials Horizons, 5 (2018) 323-343.
[2] F. Cansell and C. Aymonier, The Journal of Supercritical Fluids, 47 (2009) 508-516.
[3] J. H. Kim et al., Advanced Functional Materials, 30 (2020) 1902049.
[4] N. M. Al-Hada et al., Journal of Materials Research and Technology, 11 (2021) 252-263.
[5] C. Karakaya, Bilkent University, 2012.
[6] M. Gong, Stanford University, 2016.
[7] N. M. Noah, Journal of Nanomaterials, 2020 (2020).
[8] M. Vargas, The University of Texas at El Paso, 2015.
[9] E. Absi, M. Saleh, N. M. Al-Hada, K. Hamzah, A. M. Alhawsawi, and E. M. Banoqitah, Applied Physics A, 127 (2021) 1-32.
[10] N. M. Al-Hada et al., Journal of Materials Research and Technology, 11 (2021) 252-263.
[11] N. M. Al-Hada et al., IEEE Access, 8 (2020) 93444-93454.
[12] N. M. Al-Hada et al., IEEE Access, (2020).
[13] N. M. Al-Hada et al., International Journal of Nanomedicine, 12 (2017) 8309.

Malaysian Journal of Catalysis
http://mjcat.utm.my/
MJCat Research Article

Flake-like Tea-leaf-templated Magnesium Oxide for Carbon Dioxide Adsorption

Amirul Hafiiz Ruhaimi[1], Mohd Rozainee Taib[1] and Muhammad Arif Ab Aziz[1,2]*,

[1] *School of Chemical and Energy Engineering, Faculty of Engineering, Universiti Teknologi Malaysia (UTM), 81310 UTM Johor Bahru, Johor, Malaysia*
[2] *Centre of Hydrogen Energy, Institute of Future Energy, Universiti Teknologi Malaysia (UTM), 81310 UTM Johor Bahru, Johor, Malaysia*

**Corresponding Author: m.arif@utm.my*

Article history:
Received 16 February 2022
Accepted 5 April 2022

GRAPHICAL ABSTRACT

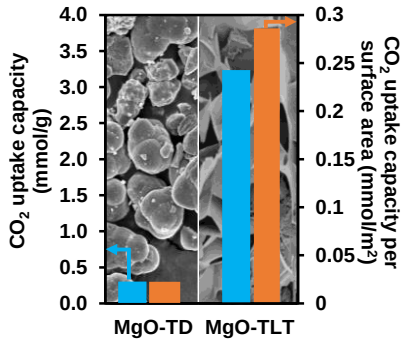

ABSTRACT

Flake-like mesoporous magnesium oxide (MgO-TLT) was prepared using a bio-templating method with tea leaves (TLTs) as the template. MgO-TLT exhibited smaller crystallites (7.52 nm) than MgO prepared using the thermal decomposition method (22.52 nm). These smaller crystallites led to more structural defects in the adsorbent and a high basic site density; consequently, MgO-TLT exhibited a high CO_2-uptake capacity of 3.17 mmol/g, which is 12-times higher than that of MgO-TD at 1 atm and 300 K, despite its low surface area. Furthermore, based on its low surface area and high uptake capacity, MgO-TLT has an uptake capacity per surface area that is more than 15-times higher than that of MgO-TD, which supports the hypothesis that MgO-TLT possesses more surface defect sites that promote the attachment of CO_2. This study revealed that TLT is a promising template for use in the bio-templating syntheses of MgO adsorbents with high surface reactivities and enhanced CO_2-uptake capacities.

Keywords: Mesoporous magnesium oxide, CO_2 adsorption, bio-templating, spend tea leaves

| eISSN 0128-2581 |

1. INTRODUCTION

Increasing concentrations of atmospheric CO_2 have attracted considerable attention owing to their long-term destructive impacts on the environment and climate. Increasing CO_2 concentrations are mainly due to uncontrolled greenhouse gas emissions from industries that consume fossil fuels [1]. Hence, several approaches for minimising CO_2 released into the atmosphere have been proposed and investigated, including carbon-capture technology. Adsorption techniques have progressively been studied as replacements for the currently widely used CO_2-capture technique that has several drawbacks, such as a high absorbent make-up rates, high energy consumption during the regeneration process [2], flow problems [3], high rates of equipment corrosion due to the formation of acidic chemicals, the loss of amines due to the presence of SO_2, NO_2, and O_2, and evaporation [4, 5]. On the other hand, adsorption is a superior technique in terms of cost efficiency, facile operational conditions, environmental friendliness, and recyclability [6].

A number of adsorption techniques that use metal-oxide-based adsorbents have been studied with the aim of identifying the structural properties required to achieve high CO_2-uptake capacities. Theoretically, a metal-oxide adsorbent, such as MgO, has a high uptake capacity for CO_2 of around 24.8 mmol/g [7]. However, the poor structural properties of common MgO, including its low adsorbent surface area and surface basicity, result in a low CO_2-uptake capacity because CO_2 cannot effectively access the active sites of the adsorbent [8]. While numerous studies aimed at improving the structural properties of adsorbents have been reported, current high-surface-area synthesis methods that use surfactants, such as cetyltrimethylammonium-bromide (CTAB), as templates, are costly because surfactant templates are expensive and the synthesis procedures are complex [9, 10]. Therefore, using a biomass-based (biomaterial-based) template represents an attractive alternative approach because such biomaterial templates can

generate adsorbents with unique structural and textural properties.

A number of studies have been documented benefiting from the bio-templating approach in various applications. For instances, by using cotton [11-13], Arabic gums [14], palm olein [15], paper fibre [16], rose petal [17-19], eggshell membrane [6, 20, 21], citrus peel [22, 23], etc… The prepared material obtained from the bio-templating method has demonstrated decent physicochemical properties in term of surface area and surface reactivity, which improved the performance, in particular for CO_2 adsorption application [6, 20, 22]. With this background in mind, the author has considered utilising the spent tea leaves as a biomaterial template in this CO_2 capture application. Due to highly consumed drinks worldwide with 18 – 20 billion cups of tea daily, plenty of spent tea leaves was generated from industry and households that were released into the environment as waste without any economic value [24]. Thus, beneficiation of the spent tea leaves (STL) is highly desired. Accordingly, to date number of studies have been conducted utilising STL in several applications, such as in the separation process, particularly as the main component or as an enhancement supporting material [24-27]. The consideration of utilising STL in addition to highly-available sources might possibly be on account of the STL's morphology features; it is reported possessing a diversified, coarse and highly porous surface composed of numerous fibrous bonds and spongy formations [28]. This could result in the final STL-used material with decent textural properties, which further influenced the performance.

Hence, in this study we fabricated a MgO adsorbent using tea leaves (TLTs) as the biomaterial template. Moreover, we also synthesised a MgO adsorbent using the thermal decomposition (TD) method and compared the physicochemical properties and uptake capacities of the MgO-TLT and MgO-TD adsorbents using FESEM, XRD, N_2 physisorption, FTIR-KBr, and TGA characterisation techniques. The CO_2-uptake capacities of the prepared adsorbents were investigated using flowing pure CO_2 at ambient pressure and temperature.

2. EXPERIMENTS

2.1 Adsorbent preparation

TLT bio-templating was initiated by immersing TLTs in boiling water several times to remove any colour residue remaining in the TLTs. The filtered TLTs were then placed in a beaker and dried overnight at 383 K. Mg $(NO_3)_2{\cdot}6H_2O$ (20 g; QRëC, 99.5%) was dissolved in ethylene glycol (EG) (200 mL; QRëC, 99.5%) with stirring and then sonicated for 10 min. Dried TLTs (5 g) were then immersed in the solution and stirred for 1 h at room temperature. Aqueous ammonia solution (5 mL, QRëC, 28%) was then added, with stirring continued for another 30 min. The TLT adsorbent was then collected by filtration, dried for 1 h at 373 K, and calcined at 823 K for 3 h. The prepared adsorbent is referred to as "MgO–TLT". MgO-TD was prepared by preheating Mg $(NO_3)_2{\cdot}6H_2O$ at 373 K for 1 h after which it was calcined at 823 K for 3 h.

2.2 Characterising the adsorbent and examining its CO_2 adsorption properties

Each adsorbent was subjected to FESEM (ZEISS Crossbeam 340) to examine its morphology, and XRD (Rigaku SmartLab with Cu Kα radiation) in the 2–90° 2θ range to investigate its crystallinity. Average adsorbent crystal size was calculated using the high-intensity XRD peak and Scherrer's equation. Textural properties were evaluated by acquiring N_2-adsorption/desorption isotherms with a gas-sorption analyser (Quantachrome Instruments, Autosorb IQ, version 3.0) after pre-treating the sample at 523 K; the obtained data were analysed using 3Flex software (version 5.0). FTIR spectra of the adsorbents were obtained on a Cary 600 series spectrometer in the 400–4000 cm^{-1} range, and the prepared adsorbents were subjected to TGA in the 303–1173 K temperature range at 10 K/min under a flow of N_2 gas. Each prepared adsorbent was examined for its CO_2 uptake capacity during CO_2-adsorption testing using a fixed-bed U-shaped gas column equipped with a CO_2 analyser under a flow of pure CO_2 at 1 atm and 298 K.

3. RESULTS AND DISCUSSION

The FESEM images in Figure 1 show that the prepared MgO samples exhibit different morphological features: MgO-TD has a spherical structure (Figure 1a) that is attributable to the direct conversion of the magnesium salt into MgO during calcination. In contrast, the TLT bio-templating method led to MgO with a thin flake-like structure (Figure 1b); this morphology is possibly associated with the use of ethylene glycol during preparation. Ethylene glycol is a promising chelating agent for polyols due to its two hydroxyl groups (-OH) [29, 30]. During synthesis, bonds can form between two or more binding sites with the same ethylene glycol ligand and a single central metal atom to form an intermediate metal-polyol complex [29] in a process known as "chelation". The following mechanism for the formation of the intermediate metal-polyol complex during $Mg(NO_3)_2$ dissolution in ethylene glycol is proposed:

$$(CH_2OH)_2 + Mg(NO_3)_2 \rightarrow Mg(OCH_2)_2 + 2HNO_3 \qquad (1).$$

As reported previously, the use of ethylene glycol and a Mg salt can result in the formation of magnesium ethylene glycolate, as an intermediate metal-polyol complex, which is then converted into MgO during calcination [6]. According to several studies, the use of a polyol (i.e., ethylene glycol) as the solvent for the MgO adsorbent results in the formation of flake-like or flower-like structures with

thin flake-like petal features or other similar structures [6, 30-32]; a flake-like structure was formed instead of a flower-like structure in this study, which is possibly be due to the attachment of magnesium ethylene glycolate to the TLT surface [30-32]. The thin flake-like structure exhibited by the MgO adsorbent is reportedly beneficial because it lowers the diffusion-resistance layer and improves MgO-use efficiency, which is expected to enhance the CO_2-adsorption performance of the adsorbent [33].

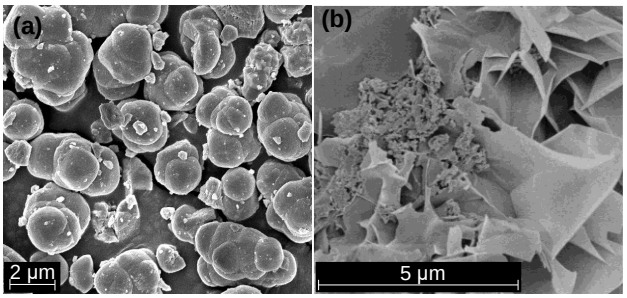

Figure 1. FESEM images of a) MgO-TD and b) MgO-TLT.

The XRD pattern of MgO-TD (Figure 2a) reveals a series of diffraction peaks at 2θ = 36.8°, 42.8°, 62.2°, 74.6°, and 78.6° that can be assigned to the (111), (200), (220), (311), and (222) crystal planes of the cubic fluorite MgO structure [34]. Moreover, MgO-TLT exhibits roughly the same diffraction peaks, although with significantly less intense; these weaker peaks are consistent with smaller crystallites. In addition, the (200) peak of MgO-TLT displayed a shifting to lower 2θ value, which indicates an expansion to a higher lattice parameter [35]. The average crystallite sizes of the prepared adsorbents were calculated using the Scherrer equation, with the (200) peak as a reference. MgO-TD was found to possess larger crystallites (19.30 nm) than MgO-TLT (4.94 nm); hence, we conclude that the use of TLT as a template produced an adsorbent with smaller crystallites than that prepared by the thermal decomposition method or previously reported bio-templated MgO (14.31 nm) [6]. On the other hand, through William-Hall (W-H) plotting (Figure 2b), where the crystallite size of both MgO-TD and MgO-TLT adsorbents are slightly different compared to Scherrer calculation, which 17.95 nm and 3.82 nm, respectively. Through W-H methodology, XRD peak broadening controlled by both size and the lattice strain could be appropriately expressed by Williamson–Hall equation (1) below [36]:

$$\frac{\beta cos\theta}{\lambda} = \frac{1}{D} + \eta \frac{sin\theta}{\lambda} \qquad (1)$$

Where λ is the x-ray wavelength of the equipment used (0.1589), θ is the peak position (radians), η is an order of refraction, λ is the x-ray wavelength (0.1589), β is the line broadening at half maximum intensity (FWHM) (radians), D is the effective crystallite size (nm), and η is the effective strain. The y-intercept and the slope of the linear fitting indicate the effective crystallite size (1/D) and effective strain (η), respectively. As depicted in Figure 2b, both adsorbents exhibited a negative slope (strain, η), indicating a compressive strain (lattice shrinkage), whereas a positive slope is the signature of tensile strain [14, 37]. According to many reports, the negative slope is encountered when the crystallite size of the sample is small, less than 20 nm [38].

The difference in crystallite size obtained through the Scherrer method and W-H plotting is owing to the consideration of the lattice strain to the peak broadening.

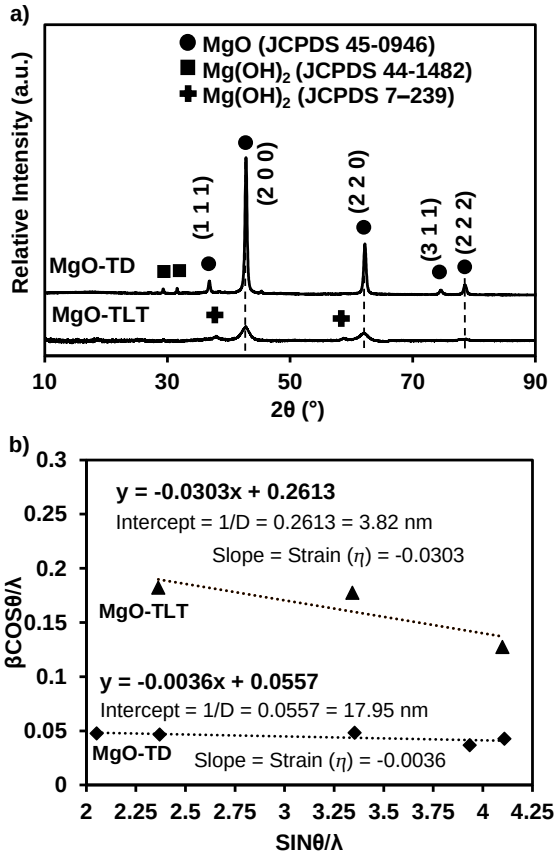

Figure 2. a) XRD patterns and b) Williamson-Hall (W–H) plot of the MgO adsorbent

Moreover, to further understand the nanocrystallite structure of the prepared adsorbent derived from the XRD profile, the estimation of lattice strain (ε) and dislocation density (δ) was performed. The effect of bio-templating on the dislocation density and strain of the prepared MgO was investigated using Eqs. (2) and (3), respectively, [39].

$$\delta = \frac{1}{D^2} \qquad (2)$$

$$\varepsilon = \frac{\beta}{4 \tan \theta} \quad (3)$$

As presented in Table 1, MgO-TLT shows higher dislocation values and strain than MgO-TD, which inversely interdependence to the crystallite size. The reason for the high lattice strain of MgO-TLT is proposed to be the influence of grain boundary. According to Shafi and Bose, for the smaller size nanostructured material, a grain boundary is associated with more volume defects like vacancies and vacancy clusters [40]. Where the stress field results from the volume defects at the grain boundaries exert lattice strain in nanostructured materials. This is also influenced by the internal pressure exerted by the surface tension on the nanomaterial, which will create a stress field inducing a lattice strain.

Table 1. The estimation of the nano-structural parameters of prepared MgO.

Lattice planes	2θ (°)	β (°)	D(nm)*	δ x 10^{-3} (nm^{-2})	ε x 10^{-3}
MgO-TD					
(1 1 1)	36.85	0.44	18.92	2.79	5.80
(2 0 0)	42.83	0.44	19.30 (17.95)	2.68	4.92
(2 2 0)	62.22	0.50	18.67	2.87	3.59
(3 1 1)	74.60	0.41	24.58	1.65	2.33
(2 2 2)	78.55	0.49	21.07	2.25	2.60
Average				**2.45**	**3.85**
MgO-TLT					
(2 0 0)	42.70	1.73	4.94 (3.82)	40.98	19.27
(2 2 0)	61.97	1.83	5.07	38.87	13.27
(2 2 2)	78.33	1.45	7.06	20.04	7.77
Average				**33.30**	**13.44**

* : Scherrer calculation

Values in parenthesis are the estimation of crystallite size using W-H methodology

Based on the above discussed nano-structural parameter, it is believed that the smaller MgO-TD crystallite size was associated with the presence of a higher structural defect site in the adsorbent then promotes high CO_2 uptake capacity [41]. This finding was supported by a previously reported study, where the egg-shell membrane (ESM) bio-templating method has resulted in the MgO-ESM adsorbent with a smaller crystallite size than the conventional thermal conversion method [6]. Furthermore, through a CO_2-TPD analysis of the above-mentioned study, it is found that flake-shaped MgO-ESM with small crystallite size demonstrated much stronger surface basicity than thermally converted MgO. This is possibly contributed by the presence of high basic site density. Moreover, this MgO-TLT finding was also consistent with several related studies in which bio-templating methods reportedly resulted in smaller adsorbent crystallites [20, 22] that significantly improved the adsorption uptake capacity.

Figure 3 shows FTIR spectra of the MgO-TD and MgO-TLT adsorbents. Both adsorbents exhibit approximately the same transmittance bands in their spectra; those at 3692 and 3460 cm^{-1} are assigned to the stretching vibrations of hydroxyl groups on crystal faces with low-coordination or defect sites, and residual moisture, respectively [42, 43]. The acquired spectra show that MgO-TLT contains a large amount of moisture. Moreover, both adsorbents exhibit bands located at approximately 1640 cm^{-1} that is associated with the bending mode of the hydroxyl groups of adsorbed molecular water attached at hydroxide and magnesia surfaces of the adsorbents [44]. In addition, the strong band observed at 1418–1490 cm^{-1} in the spectrum of MgO-TLT is attributable to the asymmetric stretching vibrations of CO_3^{2-}, which is possibly associated with carbonate species formed on the adsorbent surface [45, 46]. MgO-TD also exhibited the same CO_3^{2-} band; however, this band is less intense than that observed for MgO-TLT. This indicates that MgO-TLT is able to adsorb (via chemisorption attachment) more CO_2 from the atmospheric surrounding than MgO-TD. This likelihood could possibly be influenced by the high surface reactivity of the adsorbent, which is promoted by the present rich surface defects, i.e. cationic vacancies site (Mg^{2+}) and low-coordination anionic sites (O^{2-}) on MgO-TLT [47]. In addition, the vibrational bands observed at 862 and 550 cm^{-1} are attributable to bonds in cubic MgO and the Mg-O-Mg stretching mode, respectively [48, 49].

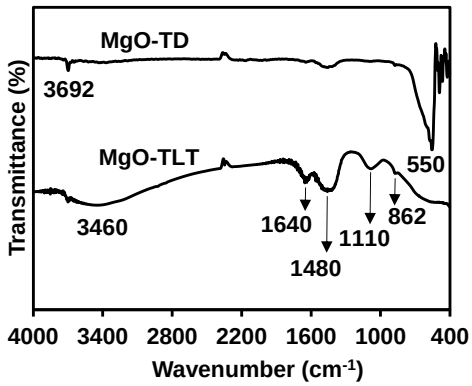

Figure 3. FTIR spectra of the prepared MgO adsorbents.

According to the N_2-adsorption–desorption isotherms, which are used to assess textural properties (Figure 4), both MgO adsorbents exhibit type-IV isotherms with H3-type hysteresis loops that indicate the presence of slit-shaped mesoporous structures [32]. MgO-TLT was found to have a slightly smaller BET surface area (11.27 m^2/g) than MgO-TD (13.63 m^2/g). This could possibly be associated with the

TLT bio-template material used, where TLT's morphological and surface functional features do not provide a significant role in the bio-templating approach. Unlike the previously studied ESM bio-templating approach, in which the interconnected fibrous network structure of the ESM with an abundant surface functional group has contributed to the enhancement of the bio-templated adsorbent structural properties [6, 20]. Moreover, the pore volume of MgO-TLT (0.007 cm^3/g) is also smaller than that of MgO-TD (0.06 cm^3/g). Although, it is worth noting that these inferior textural properties did not directly influence the CO_2 capture performance of the adsorbent. The presence of small average pore width of MgO-TLT with 6.4 nm is found beneficial for CO_2 uptake performance compared to MgO-TD with 17.5 nm. This could possibly be associated with the adsorbate-adsorbate (gas-gas) and adsorbate-adsorbent (gas-MgO) interaction. According to Ma et al., decreases in pore width will increase the CO_2 uptake densities of the adsorbent, in-which attributed to the strongly adsorbate-adsorbate and adsorbate-adsorbent interaction [50]. This consequently results in increasing adsorption heat which indicates the strong adsorption potential. Thus, improving the adsorbent's CO_2 capture.

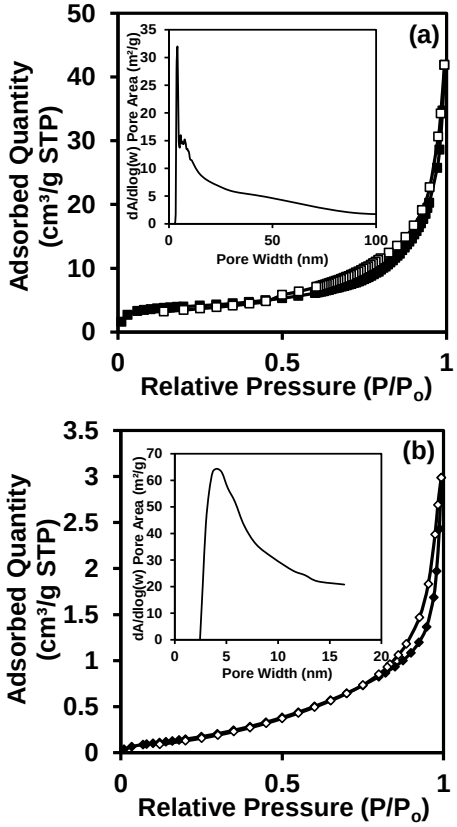

Figure 4. N_2-adsorption–desorption isotherms for a) MgO-TD and b) MgO-TLT. The insets show pore distribution curves.

As shown in Figure 5(a, b), MgO-TD and MgO-TLT exhibit very similar thermal decomposition pattern that includes three degradation stages, with water, organic compounds, and trapped carbonaceous residues removed in the first (< 513 K), second (513–773 K), and third stages (>773 K), respectively. Yet, the intensity of the weight loss is different, where the overall evaluation has shown that MgO-TD demonstrated more weight (38%) than MgO-TLT with 23%. This high weight loss observed for MgO-TD is possibly due to the large amount of organic residue present in the adsorbent, which is supported by an intense second-stage derivative weight-loss curve. Moreover, in the first and third stages, both MgO adsorbents have displayed a similar weight loss with a mostly similar derivative weight-loss curve.

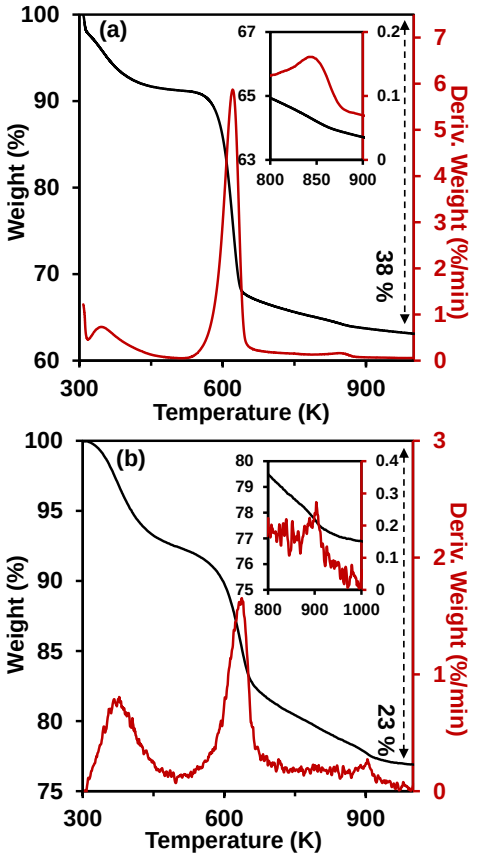

Figure 5. TGA profiles of a) MgO-TD and b) MgO-TLT. (Insert: Close-up scale of TGA profile of MgO-TD on the 3rd degradation stage)

CO_2-adsorption experiments were used to examine the association between the physicochemical properties and the CO_2-uptake capacity of each adsorbent. As depicted in Figure 6, MgO-TLT exhibited a significantly larger CO_2-uptake capacity (3.17 mmol/g) than MgO-TD (0.25 mmol/g), despite its low surface area. Moreover, the CO_2-uptake efficiency per surface area of MgO-TLT was determined to be around 0.28 $mmol/m^2$, which is almost 16-

times higher than that of MgO-TD, and it is possibly associated with superior physicochemical properties of MgO-TLT, as evidenced by the characterisation data presented above; small crystallite size and pore width. The smaller crystallites of MgO-TLT compared to those of MgO-TD (XRD section) may provide more structural defects in the adsorbent that result in a high basic site density [41]. This could also be supported by the presence of an intense band associated with adsorbed atmospheric CO_2 (FTIR section). Hence, we conclude that the TLT bio-templating method developed in this study resulted in the fabrication of MgO-TLT with significantly superior CO_2-uptake capacity despite its lower surface area.

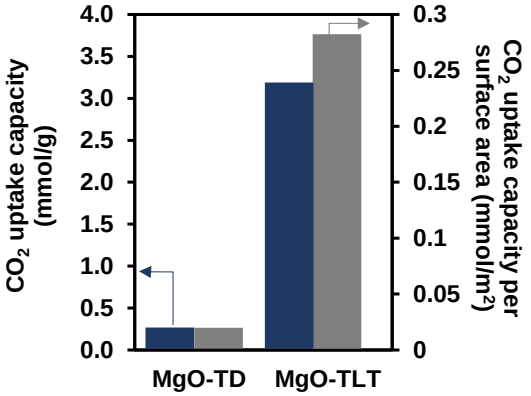

Figure 6. CO_2-uptake capacities of the MgO adsorbents.

4. CONCLUSION

In this study, we successfully synthesised mesoporous flake-like MgO-TLT using TLT as a template. TLT bio-templating resulted in the fabrication of MgO with a highly reactive surface, as evidenced by FTIR spectroscopy, which revealed bands that correspond to carbonate species formed by the attachment of atmospheric CO_2 to the MgO-TLT surface. In addition, despite its smaller surface area compared to that of MgO-TD, as well as several studies that report the same morphological features, MgO-TLT exhibited a high CO_2-uptake capacity of 3.17 mmol/g, which is 12-times higher than that of MgO-TD. Moreover, MgO-TLT also exhibited a high uptake capacity per surface area that is more than 15-times higher than that of MgO-TD and is ascribable to its high surface reactivity. Therefore, this study revealed that tea leaves are a promising and low-cost template source for the fabrication of MgO with a high CO_2-uptake capacity.

ACKNOWLEDGEMENTS

This work was supported by the Universiti Teknologi Malaysia (Grant No. 08G94) and the Ministry of Higher Education Malaysia through Fundamental Research Grant Scheme (FRGS) Grant No. FRGS/1/2019/STG07/UTM/02/8 (Grant No. 5F217).

REFERENCES

[1] J.D. Shakun, P.U. Clark, F. He, S.A. Marcott, A.C. Mix, Z. Liu, B. Otto-Bliesner, Nature 484(7392) (2012) 49.
[2] Q. Lai, Z. Diao, L. Kong, H. Adidharma, M. Fan, Appl. Energy 223 (2018) 293.
[3] A. Azmi, M. Aziz, J. Environ. Chem. Eng. 7(2) (2019) 103022.
[4] M. Aghaie, N. Rezaei, S. Zendehboudi, Renew. Sust. Energ. Rev. 96 (2018) 502.
[5] L. Jiang, A. Gonzalez-Diaz, J. Ling-Chin, A. Roskilly, A. Smallbone, Appl. Energy 245 (2019) 1.
[6] A.H. Ruhaimi, M.A. Ab Aziz, J. Solid State Chem. 300 (2021) 122242.
[7] W. Gao, T. Zhou, Y. Gao, B. Louis, D. O'Hare, Q. Wang, J. Energy Chem. 26(5) (2017) 830.
[8] A.H. Ruhaimi, M.A.A. Aziz, A.A. Jalil, J. CO_2 Util. 43 (2021) 101357.
[9] L. Wang, J. Zhang, F. Chen, Micropor. Mesopor. Mat. 122(1) (2009) 229.
[10] B. Abarna, T. Preethi, A. Karunanithi, G. Rajarajeswari, Mater. Sci. Semicond. Process. 56 (2016) 243.
[11] Y. Tang, Z. Li, Z. Xu, J. Zhang, C. Qu, Z. Zhang, RSC Adv. 10(48) (2020) 28695.
[12] J.J. Huang, C.C. Wang, L.T. Jin, F. Chen, Z.G. Chen, Trans. Nonferrous Met. Soc. China 27(3) (2017) 578.
[13] Z. Jia, G. Luo, H. Wu, Z. Li, T. Ni, M. Ai, Solid State Sci. 94 (2019) 120.
[14] S. Taghavi Fardood, A. Ramazani, S. Woo Joo, J. Appl. Chemical Research 12(1) (2018) 8.
[15] D. Ramimoghadam, M.Z.B. Hussein, Y.H. Taufiq-Yap, Chem. Cent. J. 7(1) (2013) 71.
[16] X. Ma, Y. Li, X. Yan, W. Zhang, J. Zhao, Z. Wang, Chem. Eng. J. 361 (2019) 235.
[17] J. Yang, M. Wang, S. Zhao, Y. Liu, W. Zhang, B. Wu, Q. Liu, Int. J. Hydrog. Energy 44(2) (2019) 870.
[18] A. Chen, J. Qian, Y. Chen, X. Lu, F. Wang, Z. Tang, Powder Technol. 249 (2013) 71.
[19] B. Wu, C. Shan, X. Zhang, H. Zhao, S. Ma, Y. Shi, J. Yang, H. Bai, Q. Liu, Appl. Surf. Sci. 543 (2021) 148677.
[20] A.H. Ruhaimi, M.A. Ab Aziz, Chem. Phys. Lett. 779 (2021) 138842.
[21] A.H. Ruhaimi, M.A.A. Aziz, Appl. Phys. A 128(1) (2022) 1.
[22] A.H. Ruhaimi, C.C. Teh, M.A.A. Aziz, Bull. Chem. React. Eng (2021) 16(2), 366.
[23] B. Su, M. Zhong, L. Han, M. Wei, Y. Liu, H. Yang, Z. Lei, Mater. Res. Bull. 124 (2020) 110777.
[24] M.A. Ahsan, M.A. Imam, A.R. Puente Santiago, A. Rodriguez, B. Alvarado-Tenorio, R. Bernal, R. Luque, J.C. Noveron, Green Chem. 22(20) (2020) 6967.
[25] S. Wong, H.H. Tumari, N. Ngadi, N.B. Mohamed, O. Hassan, R. Mat, N.A. Saidina Amin, J. Clean. Prod. 206 (2019) 394.
[26] Y.P. Chen, C.H. Zheng, Y.Y. Huang, Y.R. Chen, Chemosphere 286 (2022) 131770.
[27] M. Nur-E-Alam, M. Abu Sayid Mia, F. Ahmad, M. Mafizur Rahman, Appl. Water Sci. 8(5) (2018) 129.
[28] J.O. Ighalo, A.G. Adeniyi, SN Appl. Sci. 2(3) (2020) 509.
[29] N. Abdullah, N. Osman, S. Hasan, O. Hassan, Int. J. Electrochem. Sci. 7 (2012) 9401.
[30] P. Li, R. Chen, Y. Lin, W. Li, Chem. Eng. J. 404 (2021) 126459.
[31] J.H. Lee, H. Jeon, J.T. Park, J.H. Kim, Biomass Bioenerg. 142 (2020) 105788.
[32] P. Li, Y. Lin, R. Chen, W. Li, Dalton Trans. 49(16) (2020) 518.
[33] Y. Guo, C. Tan, P. Wang, J. Sun, W. Li, C. Zhao, P. Lu, Chem. Eng. J. 379 (2020) 122277.
[34] K. Nemade, S. Waghuley, Int. J. Met. (2014).
[35] A.D. Prasetya, M. Rifai, Mujamilah, H. Miyamoto, J. Phys. Conf. Ser. 1436(1) (2020) 012113.
[36] B. Choudhury, A. Choudhury, Mater. Chem. Phys. 131(3) (2012) 666.
[37] A. Khorsand Zak, W.H. Abd. Majid, M.E. Abrishami, R. Yousefi, Solid State Sci. 13(1) (2011) 251.
[38] K. Maniammal, G. Madhu, V. Biju, Physica E Low Dimens. Syst. Nanostruct. 85 (2017) 214.

[39] K. Igenepo John, A. Abdul Adenle, A. Timothy Adeleye, I. Pearl Onyia, C. Amune-Matthews, M.O. Omorogie, Chem. Phys. Lett. 776 (2021) 138725.
[40] P.M. Shafi, A.C. Bose, AIP Adv. 5(5) (2015) 057137.
[41] K.K. Han, Y. Zhou, W.G. Lin, J.H. Zhu, Micropor. Mesopor. Mat. 169 (2013) 112.
[42] N.C.S. Selvam, R.T. Kumar, L.J. Kennedy, J.J. Vijaya, J. Alloys Compd. 509(41) (2011) 9809.
[43] H. Jeon, Y.J. Min, S.H. Ahn, S.M. Hong, J.S. Shin, J.H. Kim, K.B. Lee, Colloids Surf. A: Physicochem. Eng. Asp. 414 (2012) 75.
[44] I.F. Mironyuk, V.M. Gun'ko, M.O. Povazhnyak, V.I. Zarko, V.M. Chelyadin, R. Leboda, J. Skubiszewska-Zięba, W. Janusz, Appl. Surf. Sci. 252(12) (2006) 4071.
[45] J. Sivasankari, S. Selvakumar, K. Sivaji, S. Sankar, J. Alloys Compd. 616 (2014) 51.
[46] L. Hopkinson, P. Kristova, K. Rutt, G. Cressey, Geochim. Cosmochim. Acta. 76 (2012) 1.
[47] D. Ochs, M. Brause, B. Braun, W. Maus-Friedrichs, V. Kempter, Surf. Sci. 397(1-3) (1998) 101.
[48] I.W. Sutapa, A.W. Wahab, P. Taba, N. La Nafie, Orient. J. Chem. 34(2) (2018) 1016.
[49] S. Aksay, Phys. B: Condens. Matter 570 (2019) 280.
[50] X. Ma, Y. Wu, M. Fang, B. Liu, R. Chen, R. Shi, Q. Wu, Z. Zeng, L. Li, Biomass Bioenerg. 158 (2022) 106353.

Malaysian Journal of Catalysis
http://mjcat.utm.my/
MJCat Research Article

Biodiesel Synthesis Via Transesterification Reaction Using Chemically-Based Heterogenous Catalysts Under Microwave Irradiation

Abdelmalik Milad Shakorfow[1*] and Elham Milad Daribi[1]

[1] *Chemical and Petroleum Engineering, Faculty of Engineering, Elmergib University, Khoms- Libya*

Corresponding Author:* ***Dr_Eng.Malik@Yahoo.Co.Uk*

Article history :
Received 2 April 2022
Accepted 1 Jun 2022

ABSTRACT

This review paper has reviewed, albeit not thoroughly, biodiesel synthesis via transesterification reaction of non- edible and waste oils using chemically- based heterogenous catalysts induced by microwave irradiation. Synthesis of biodiesel from such feedstock oils can help boost biodiesel commercialization since it is an economical alternative to fresh edible oils in order to reduce the cost of raw materials. Another cost cut- off might arise from the use of heterogenous catalysts with microwave heating which consumes less energy and requires a shorter transesterification reaction time with a better reaction kinetics without compromising the overall biodiesel yield, in comparison to conventional heating. Results of the reviewed work have indicated that microwave heating could outperform conventional heating in all aspects considered, although reaction conditions are moderated in the former mode of heating. Also, it has been observed that acceleration of a transesterification reaction by microwave heating cannot be compared to that under conventional heating under; otherwise, identical reaction conditions. In addition, microwave- assisted heterogeneously- catalyzed transesterification reactions are featured with the generation of hot- spot zones, superheating and selective species heating. Out of these phenomena, the efficiency of heating process is increased; thus, rate of transesterification reaction is accordingly increased while production of by- products is decreased. The performance of heterogenous catalysts in catalyzing transesterification reactions, with their high reactivity, stability and selectivity under the influence of microwaves, has been superb.

Keywords: transesterification, free fatty acid, microwaves, heterogenous, impregnation.

| eISSN 0128-2581 |

1. INTRODUCTION

Due to its environmental benefits including biodegradability and nontoxicity, biodiesel, as an alternative to classical fossil fuels, has become a more attractive fuel. Due to some challenges, commercialization of biodiesel synthesis through catalytic transesterification reaction has not been significantly effective; however. Of these challenges are: high operating cost, low production efficiency due to kinetic limitations, high energy consumption, long time and complication of product-catalyst separation and high cost as well as lack of sustainability of raw material(s), fresh edible oils, used as a feedstock for biodiesel synthesis. Such oils include but not limited to oils of: barley, canola, coconut, copra, corn, cotton seeds, ground nut, oat, palm, rape seed, rice, safflower, soybean and wheat. To slightly overcome such challenges, biodiesel has been synthesized based on the use of waste cooking oils which are of no value and can environmentally be a burden if; otherwise, disposed off. Also, another alternative has been the use of non- edible oils such as oils of: almond, babassu, jatropha curcas, palm, rice bran, sesame, salmon and tobacco seeds, etc.

Transesterification (alcoholysis) is a reversible modification reaction out of which glycerol is removed from the triglycerides of the starting feedstock oil/fat in the presence of a catalyst to produce the corresponding fatty acid alkyl esters (biodiesel) with respect to the alcohol used [1-5]. A typical transesterification reaction in which methanol (methanolysis) is employed as an alcohol is depicted in Fig. (1).

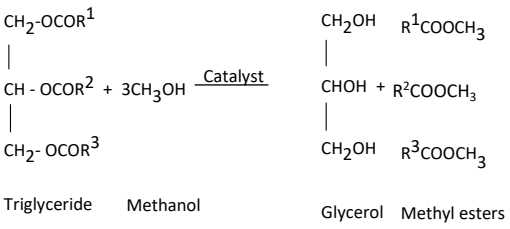

Fig. (1): Transesterification Reaction, redrawn from Ejikeme, et al. [5].

In order for a catalytic transesterification reaction to progress: 1- a catalyst of a certain characteristics must be used unless the route followed is the supercritical heating mode which is non- catalytic and 2- a certain temperature has to be maintained depending on the feedstock oil/fat as well catalyst used. Catalysts in use for transesterification reactions for biodiesel synthesis have included: enzymes [6], homogenous [7] and heterogenous [8-9]. In general, heterogenous catalysts for biodiesel synthesis require drastic reaction conditions: reaction temperatures reach up to 476 °C, catalyst amount up to 10 wt.% and alcohol to oil molar ratio between 10:1 and 25:1 or even higher. These harsh costly conditions are required in order to make- up low mass transfer rates due to small surface area of such catalysts by which a low contact with the reactants is caused. Thus, to achieve a certain biodiesel yield, reaction duration has to be prolonged. Other issues that may arise due to using heterogenous catalysts to catalyze a transesterification reaction include: poisoning, sintering, coking and leaching by which deterioration of the catalytic reactivity of the catalyst is inevitable. High cost and difficulty of removal of small catalyst particles via filtration from the produced biodiesel are also hurdles that might limit use of heterogenous catalysts in this application. Nevertheless, heterogenous catalysts; in general, are tolerant to oils with high levels of free fatty acids and water, as the case with waste feedstock oils, when used for biodiesel synthesis, resulting in no formation of undesirable soap. Also, use of such heterogenous catalysts in biodiesel synthesis could ensure no corrosion effects on equipment used. Heterogenous catalysts are also featured with high reactivity, stability, selectivity as well as long lifetime; in particular, if a solid material support is integrated in their design such as alumina or silica, etc. Another good feature of such catalysts is their regeneration for subsequent use(s) exhibiting no or trivial catalytic deterioration. Besides, product (biodiesel) purification, which is costly and complicated, can; to a large extent, be eliminated if heterogenous catalysts are employed [9].

Equally crucial is maintaining the be-spoke temperature throughout the transesterification reaction to ensure the progress of the reaction. Nature of the feedstock oil/fat as well as catalyst used, *do* play a role in deciding the transesterification reaction's temperature. In order to attain the required temperature, some sort of heat must be supplied to the transesterification reaction mixture. Heating can be via conventional, supercritical or non- conventional modes. Among non- conventional modes are: ultrasonic, plasma and microwaves (dielectric). Of these modes, microwaves are further examined in this review. Whilst applying the conventional heating (wall heating), in which, as previously mentioned, a certain catalyst of a certain type must be used, which usually requires a separation procedure unless being heterogenous, transesterification reaction temperature is between 60 and 476 °C with atmospheric pressure being sufficient. In terms of heat loss, it is evident since heat is lost to the environment via conduction and convection while transferring heat through reactor's wall and reactants; respectively [10-11]. One additional problem of conventional heating is that it creates a non- uniform temperature distribution through the heated medium. Also, properties of the heated medium, e.g., density, heat capacity and thermal conductivity play a major role in the efficiency of heating. However, in supercritical heating mode, there is no need to use a catalyst; thus, there is no procedure required for catalyst removal. Absence of the catalyst(s) is; however, supplemented by the employment of severe reaction conditions of too high pressure and temperature, up to 60 MPa and 400 °C; respectively. This can be a safety concern and requires a high capital cost. The need to use a catalyst, at certain reaction conditions of pressure and temperature as the case with conventional heating, is again what features microwave heating. However, heat loss is minimal since heating the reactor's wall is not involved and that molecules of the entire liquid within the heated medium are subjected to microwaves which constitute electric and magnetic fields each of which interact differently with molecules to be heated [11]. This is governed by ionic conduction and one kind of dipolar polarization whether displacement, orientation or interfacial polarization. In microwave heating, almost 65% of electrical energy can be converted into heat via a microwave equipment [12]. In addition, microwave heating is advantageous over conventional and supercritical heating modes in terms of short reaction time [13], higher process efficiency and cleaner products [11,14-18]. To this end, use of microwaves as a heating means has seen versatile applications including: biodiesel synthesis, methane conversion, coal and biomass conversion, desulfurization and carbon dioxide separation, materials synthesis, etc. [12]. The aim of this paper is to review the research published on biodiesel synthesis from different non- edible and waste oils via transesterification reaction using different chemically-based heterogenous catalysts under microwave irradiation. For comparison purposes, use of conventional heating in this regard is touched upon.

2. Biodiesel Synthesis Via Chemically-Based Heterogenous Catalysts Under Microwave Irradiation

Basic and Acidic heterogenous catalysts have been synthesized based on chemical material(s) and recently

based on the use of waste materials. Use of acidic chemically- based heterogenous catalysts in the synthesis of biodiesel has been reviewed elsewhere [9]. Investigations reported in this review were all, opposing to this current review, relying on conventional heating methods to facilitate the desired transesterification reaction's temperature [9]. This paper; however, focuses on the employment of such heterogenous catalysts for the purpose of transesterification of different non- edible and waste oils under microwave heating. Microwaves are electromagnetic waves that form when electric and magnetic fields are coupled perpendicularly to each other. Among the electromagnetic spectrum, microwaves sit at the middle between radio waves and infrared waves. The wavelengths of microwaves range from 0.01 to 1 m. Frequencies of microwaves are broad and extend thousand times from 0.300 to 300 GHz, although most common frequencies applied industrially are between 0.915 and 2.450 GHz. Thus, a successful chosen heterogenous catalyst should be capable to absorb microwaves with such frequencies beyond its skin depth. In terms of frequency, wavelength and energy content, microwaves with higher frequencies possess shorter wavelengths while a higher energy content. Also, the response of materials exposed to microwaves varies from a material to another according to their polarity, viscosity, density, temperature, concentration and molecular wight [12]. To avoid digression, further details on principles, theory and mechanism of microwave heating, the requirement(s) of equipment used with microwave heating and microwaves- assisted organic reactions are left to the reader and can be found elsewhere [19-20].

In order to enhance the synthesis process of biodiesel, Kord and his coworkers have investigated the transesterification reaction of castor oil under microwave irradiation while using methanol as an alcohol and KOH as a heterogenous catalyst. The alcohol used and the ingredients of the catalyst used are all with high dielectric properties which are of great contribution towards absorption of microwaves. Only two minutes were required to obtain a biodiesel yield of 92.15% [21]. In another work, Yuan and co- workers have investigated the synthesis of biodiesel from castor oil under microwave irradiation. In this work, the performance of two acid homogenous catalysts and a heterogenous base catalyst, in catalyzing the transesterification reaction of castor oil with methanol, was evaluated. Acid homogenous catalysts used included $NaHSO_4.H_2O$ and $AlCl_3$ while the heterogenous base catalyst was Na_2CO_3. The required temperature for the transesterification reaction was secured by conventional heating and microwave heating. Among heating modes and catalyst used, microwave heating when used with Na_2CO_3 catalyst, biodiesel yield was the highest at 90%. In terms of energy consumption, microwave heating consumed less energy than conventional heating in all experiments carried out [22].

In another study performed by Zhang and co-workers, higher than 96% of biodiesel yield was obtained in 10 min via a microwave-aided transesterification of yellow horn oil using 1 wt.% of heteropolyacid as a catalyst and methanol as an alcohol [23]. Using the same alcohol, in 2011, Hsiao et al. and Patil et al. have investigated the transesterification of soybean oil and camelina sativa oil using a powder of CaO and BaO, CaO, MgO and SrO, respectively. In both works, experiments were performed under conventional heating and microwave heating. Under microwave heating, biodiesel yield was 95% and 94% out of the first and second work, respectively [24-25]. Among the catalysts used in the second work, BaO and SrO were better than CaO and MgO in terms of the obtained yield. Also, the transesterification reaction rate while performing the experiments under microwave heating was two orders of magnitude higher than that obtained in conventional heating [25]. In the same year, work on microwave- assisted transesterification of *pongamia pinnata* seeds oil was also carried out for the production of biodiesel. Methanol and two alkali heterogenous catalysts; namely, NaOH and KOH were used as an alcohol and catalysts for the transesterification reaction, respectively. A biodiesel yield of 96% via both catalysts was obtained after 5 min as the reaction started [26]. In addition, Kamath, H. V. and Saidutta, R. M. B., have synthesized biodiesel from karanja oil using methanol as an alcohol and KOH as a catalyst for the transesterification reaction under the influence of microwave heating for 150 sec. However, this was not possible unless a pretreatment procedure, via an esterification reaction for 190 sec in order to reduce the content of free fatty acids of the oil to 1.04-1.18%, was followed. Satisfactory biodiesel yield was obtained out of this work, 90% [27].

Based on ceiba pentandra oil, Silitonga, et al., have synthesized biodiesel via a microwave- assisted transesterification reaction using methanol and KOH as an alcohol and a catalyst; respectively, with agitating the reactants continuously, in order to speed- up the reaction rate and shorten the reaction time. They have obtained biodiesel in a short time with an average yield of 95.42% in an energy-efficient fashion, keeping the production at a minimum [28]. Also, Lin, J. J. and Chen, W. C., have used this alcohol and catalyst with agitation again for the transesterification of jatropha seeds oil while applying conventional and microwave heatings employing mild conditions. Transesterification reaction rate obtained via microwave heating was much faster than that when a conventional heating reactor was used [29]. Pongamia pinnata oil, which is widely available in India, has been subjected to conventional and microwave heatings in an effort to synthesizing biodiesel using the same alcohol and catalyst used in the work just reported. Due to the high content of free fatty acids of the used oil, a pretreatment procedure was necessary in order to produce biodiesel with a low acid value. Compared to conventional heating, with microwave heating, significant improvements in the yield, reaction time and processing time of the produced biodiesel were reported [30]. Also, a yield of biodiesel of 99.40% was obtained in an investigation by Choedkiatsakul and others in 1.75 min as a

reaction time of transesterification of palm oil under microwave conditions using methanol and only 1 wt. % of NaOH as a heterogenous catalyst [31].

Again, using methanol, biodiesel was also synthesized from a waste cooking oil in the presence of microwave irradiation and calcium diglyceride as a catalyst. The highest biodiesel yield reported is 94.86% obtained in 15 min [32]. In order to improve biodiesel yield based on use of a waste cooking oil, Chen and others have separately used CH_3NaO and NaOH as catalysts and methanol as an alcohol coupled with a microwave heating system. In this work, it was found that biodiesel yield increases as reaction power was increased up to 750 W. Higher reaction power(s); however, were found to be with a problematic effect on reactants molecules. Compared to NaOH, CH_3NaO was associated with higher biodiesel yield when both catalysts used at 0.75 wt.%. Reaction duration was as little as 3 min [33]. In another study, Hsiao and co- workers have compared the performance of a traditional water- heating path system and that of a microwave heating system in heating the transesterification reaction of a waste cooking oil. Methanol was used as an alcohol and a novel alkaline solid surface-modified CaO as a reaction catalyst. It was reported that, the modified CaO is characterized with a high thermal stability. Compared to the traditional water- heating bath system, with microwave heating system reaction time was significantly reduced. Also, biodiesel conversion was 98.20% while using microwave irradiation as a heating media compared to 53.66% when heating was through a traditional water- bath system, despite nearly doubling the reaction time from 75 to 140 min. In both arrangements, reaction temperature was 65 °C, methanol- to- oil molar ratio was 8:1 and concentration of CaO was 4 wt.% [34]. In another work, Hsiao and co-workers have performed a similar work using a low-quality oil with a high acid value, 4.84 mg KOH/g, in order to synthesize biodiesel via microwave heating but using NaOH as a catalyst instead of CaO. Reported conversion to biodiesel was up to 98.20% [35]. In Table (1), details of most of these above cited investigations in addition to other investigations on microwave- assisted transesterification of different non- edible and waste feedstocks employing different chemically- based heterogenous catalysts, are summarized; while, for comparison purposes, Table (2) summarizes details of some investigations previously reviewed elsewhere on transesterification of different feedstocks under conventional heating [9].

3. Performance of Chemically- Based Heterogenous Catalysts and Microwave Irradiation in Transesterification Reactions for Biodiesel Synthesis

Although satisfactory biodiesel yields have been obtained while using various efficient chemically- based heterogenous catalysts under conventional heating as reported in Table (2), conditions of transesterification reaction; however, had to be intensified in all works cited. Reaction temperature is elevated up to 476 °C, catalyst amount used is high, 10 wt.% as well as a high methanol to oil molar ratios, i.e., consumption of high amounts of methanol, up to 24:1, are used. Besides, duration of transesterification reaction ranged from two to eighteen hours. This, unfortunately, renders transesterification reaction via different chemically- based heterogeneous catalysts aided by conventional heating an energy intensive costly process.

However, based on investigations cited above, refer to Table (1), it can be observed that microwave heating is advantageous over conventional heating in terms of higher biodiesel yield and shorter time required for a transesterification reaction, with other reaction conditions are moderated. Required reaction temperature, catalyst amount and methanol to oil molar ratio are much lower than that exercised in transesterification reactions under conventional heating. In fact, as stated earlier, heterogenous catalysts are featured with high reactivity, stability and selectivity. These features could be further boosted by microwaves for the benefit of increased reaction rate, longer catalyst lifespan and increased production selectivity, respectively. The catalytic reactivity of a heterogenous catalyst is a measure of the extent of chemical bonds between its surface and reactants involved in the reaction. It depends on the structure and composition of sites on the surface of the catalyst. Microwaves with the aid of polarity of reactants molecules contribute to faster rates of rotation of these molecules leading to increased reaction rates. Furthermore; perhaps, one reason that all investigations under scrutiny have used methanol as an alcohol for transesterification reactions is its high polarity as well as its higher dielectric constant than other alcohols, that render it the fastest alcohol to heat up promoting its capability to absorb microwaves [60]. This can help improve the transesterification reaction under microwave irradiation, which as mentioned above, is governed by ionic conduction and dipolar polarization [11]. Moreover, it has been proposed that via microwave heating, inevitable catalyst deactivation, by poisoning, sintering, coking and leaching, could be retarded, i.e., a longer catalyst lifetime. The influence of microwave heating on the selectivity of a heterogenous catalyst can be understood through rapid heating rates and high temperatures that localize on certain sites on the surface of the catalyst, by which a non- uniform distribution of electromagnetic field develops, due to the presence of some metals when impregnated on the surface

Table 1 A summary of some investigations on microwave-assisted transesterification of different non-edible and waste feedstocks

Feedstock Oil	Catalyst	Transesterification Reaction Parameters				Biodiesel Yield/ Conversion, %	Reference
		Reaction Temperature, °C	Maximum Reaction Time, min	Maximum Catalyst Concentration	Methanol to Oil Molar Ratio		
Yellow horn oil	Heteropolyacid catalyst	-	10	1 wt.%	12:1	Y= 96.22	23
Palm oil	NaOH	70	1.75	1 wt.%	12:1	Y= 99.40	31
Pongamia pinnata seeds oil	NaOH	60	5	0.5 wt.%	1:6	Y= 96	26
Pongamia pinnata seeds oil	KOH	60	5	1 wt.%	1:6	Y= 96	26
Jatropha oil	Potassium fluoride modified hydrotalcite		30	10 wt.%	2:10	Y= 97	36
Jatropha curcas oil	20% KOH impregnation on CaO		68	3.17 wt.%	8.42:1	Y= 97.1	37
Soybean oil	Alumina/silica loaded with potassium sodium tartrate	65	45	8 wt.%	13:1	Y= 96.5	38
Soybean oil	Potassium hydroxide (KOH) impregnated alumina (KOH/ɣ- Al_2O_3)	65	35	3 wt.%	12:1	Y= 97.30	39
Wet microalgal biomass	Ionic liquid	-	25	-	4:1	Y= 42.22	40
Camelina sativa oil	BaO	-	4	1.5 wt.%	9:1	Y= 94	25
Soybean oil	Amorphous SiO2 loaded with 10 wt.% of sulfonic groups	-	-	1 wt.%	1:10	-	41
Waste cooking oil	Heterogeneous base catalyst- calcium diglyceroxide	62	15	1.03 wt.%	7.46:1	Y= 94.86	32
Jatropha oil	KF-Modified Natural Halloysite	-	30	Catalyst/oil:1/30	8:1	Y= 83.77	42
Waste cotton seed and cooking oil	CaO	-	9.7	1.33 wt.%	9.6:1	Y= 89.94	43
Soybean oil	Nano powder calcium oxide	60	60	3 wt.%	7:1	Y= 96.60	24
Corn oil	Diphenylammonium salt	150	20	20 mol. %	5:2, g/g	Y= 100	44
Castor oil	55% H_2SO_4/C	58	2	1.44 wt. %	7.12:1	Y= 92.15	21
Castor oil	H_2SO_4 immobilised in SiO2	60	30	10 wt. %	6:1	C= 95	45
Rapeseed oil	KSF montmorillonite	170	60	10 wt. %	9:1	Y= 51	46
Free fatty acid stearic acid	Macroporous styrene chelate resin, with -NHCH2PO3H2 functional groups	80	420	9 wt. %	11:1	C= 90	47
Waste lard fat	35% CaO/zeolite	-	1.25	8 w/v	30:1	90.89	48
Chlorella vulgaris lipid	SiC-NaOH/GO	85	5	4 wt. %	48:1	Y= 81	49
Canola oil	ZnO/La2O2CO3	85	5	1 wt. %	12:1	Y>95	50

Table 2 A summary of some investigations on transesterification of different feedstocks under conventional heating

Catalyst	Transesterification Reaction Parameters				Biodiesel Yield/ Conversion, %	Reference
	Reaction Temperature, °C	Maximum Reaction Time, min	Maximum Catalyst Concentration	Methanol to Oil Molar Ratio		
Sulfated zirconia	150	240	7.61 wt.%	9.88:1	Y= 90	51
KOH	65	120	1 wt. %	9:1	Y= 95	52
Sulfated zirconia and KOH	63.50	-	1.439 wt. %	7.472:1	Y= 84.51	53
Sulfonated poly (vinyl alcohol), SPVA, and zirconium sulfate ($Zr(SO_4)_2$),	65	120	4 wt. %	12:1	Y= 95.1	54
Tungstophosphoric acid (TPA), impregnated on four different supports such as hydrous zirconia, silica, alumina and activated carbon	200	-	3 wt. %	9:1	Y= 90	55
$AlCl_3$	100	1080	5 wt. %	24:1	C= 98	56
Zeolite	65	-	10 wt.%	16:1	Y= 84	57
Ion exchanger using natural zeolite	60	120	100 g KOH/100 ml	-	Y= 95.24	58

Table 3 Comparison Between Conventional and Microwave- Assisted Transesterification Reactions of Some Non-Edible and Waste Feedstock Oils

Feedstock Oil	Conventional Heating						Microwave Heating					
	Catalyst	Catalyst Concentration, wt. %	Molar Ratio	Reaction Temperature, C	Reaction Time, Min	Yield/Conversion, %	Catalyst	Catalyst Concentration, wt. %	Molar Ratio	Reaction Temperature, C	Reaction Time, Min	Yield/ Conversion, %
Canola Oil	$AlCl_3$	5	24:1	100	1080	C= 98	$ZnO/La_2O_2CO_3$	1	12:1	85	5	Y >95
Jatropha Curcas Oil	Sulfated Zirconia	7.61	9.88:1	150	240	Y= 90	KOH	3.17	8.42:1	-	68	Y= 97.1
Waste Oil	Zeolite	10	16:1	65	-	Y= 84	Calcium Diglyceroxide	1.03	7.46:1	62	15	Y= 94.86

of that catalyst; for instance. This has the outcome of increasing product selectivity through rapid activation of reactants [12] while reducing the production of by-product(s), i.e., a simpler and shorter time of downstream separation [61-62].

Also, in contrast to conventional heating, phenomena like generation of hot- spots, superheating and selective species heating *do* accompany microwave heating which positively influence heating process efficiency and accordingly transesterification reaction rate by which a higher biodiesel yield can be obtained in a shorter reaction time. Due to non- uniform distribution of electromagnetic field on the surface of the heterogenous catalyst, hot- spot zones generate aligning on the catalyst's surface, creating a temperature gradient between 15- 200 °C. Intensity of the formed temperature gradient largely depends on the thermal conductivity of the catalyst used. This leads to a localization of high temperatures in that region which promotes product (biodiesel) formation as a result of increased reaction rate. Also, due to the temperature gradient, product formed on the surface of the heterogenous catalyst in its active sites will have to migrate back to the bulk where the temperature is ubiquitously lower. In another study, it was found that the intensity of electric field is utmost at the point of contact

between two adjacent catalyst particles [63]. Formation of hot- spot zones is further promoted if the heterogenous catalyst used in transesterification reaction consists of metal(s) impregnated on its surface. Furthermore, due to the contact of microwaves with metal(s) involved, local micro-plasmas and electrical arc at metal sites are formed which positively affect the reaction through forming another temperature gradient within the catalyst, i.e., between the body of the catalyst and metal sites [64]. In addition, heterogenous catalyst particle geometry, morphology and content of electrically conductive particles within its matrix, all play a role in enhancing the formation of hot- spot zones. It was found that, a spiked heterogenous catalyst exhibited better dielectric properties than that of a cubed one. Understandably, conductive particles when added to the matrix of a heterogenous catalyst were found to support the formation of hot-spot zones [65]. In addition to this, minimal heat loss renders microwave heating a superb heating means. Finally, selective species heating via microwaves can be explained through different responses of metals loaded to the surface of the heterogenous catalyst to microwave irradiation. Depending on these different responses, certain part of the heterogenous catalyst (selective species) will be heated the most leading to increased reaction rate [12**].**

4. Comparison Between Conventional and Microwave- Assisted Transesterification Reactions of Some Feedstock Oils

Although yields/conversions obtained out of all microwave-assisted transesterification reactions are always higher than that obtained out of transesterification reactions of the same feedstock oils in which conventional heating is used while using different catalysts, a proximity of the values of these yields/conversions obtained can be noticed. However, this proximity is not available when comparing catalyst concentrations, methanol to oil molar ratios, reaction temperatures and times applied in both transesterification reactions. In transesterification reactions heated- up conventionally, these parameters are evidently higher by several orders of magnitude when compared to those applied in microwave- assisted transesterification. Numerical values that support this argument are displayed in Table (3).

4. CONCLUSION

High energy consumption and; thus, high operating cost, that have been among the challenges that hinder commercialization of biodiesel synthesis through catalytic transesterification by means of heterogenous catalysts, may be diminished if transesterification reaction is assisted by microwaves. This is also applicable to the time required for product- catalyst separation owing to the good features of heterogenous catalysts mentioned above. Furthermore, cost of raw materials used for biodiesel synthesis can also be reduced if waste or non- edible oils are used instead of fresh edible oils. According to results reported in works under scrutiny in this paper, yield of biodiesel based on waste and non- edible oils has not been compromised and is comparable to that obtained from fresh edible oils. Heterogeneously- catalyzed transesterification reactions heated- up by conventional heating suffer from the need of high temperatures, heat loss and non- uniform temperature distribution. In heterogeneously- catalyzed transesterification reactions supplemented by microwaves; however, reaction conditions are moderated, heat loss and reaction time are little while process efficiency is high. Shortened transesterification reaction time and high process efficiency might be attributed to the improved reaction kinetics while heating via microwaves in comparison to conventional heating. This improvement is due to the productive integration between microwaves and the high reactivity, stability and selectivity of the heterogenous catalyst used, through faster movement of reacted molecules, low catalyst deactivation and rapid heating rates and high temperatures that localize on certain sites on the surface of the catalyst, respectively. Furthermore, polarity and high dielectric constant of the used alcohol for transesterification reaction could contribute towards better reaction kinetics. Perhaps, this is the reason why all investigations under scrutiny have used methanol as an alcohol for their transesterification reactions. In addition, microwave- assisted heterogeneously- catalyzed transesterification reactions are featured with the generation of hot- spot zones, superheating and selective species heating. Out of these phenomena, the efficiency of heating process is increased; thus, rate of transesterification reaction is accordingly increased while production of by- products is decreased.

REFERENCES

[1] F. Jalal, P. S. Ilavarasi and L. R. Miranda, 2011 IEEE Conference on Clean Energy and Technology (CET), (2011) 125-128.

[2] Encinar JM, Pardal A, Sánchez N, Nogales S. Energies, 11 (2018) 2229.

[3] Meher L. C, Dharmagadda V. S., Naik S. N. Bioresour Technol. 12 (2006) 1392-1397.

[4] George Anastopoulos, Ypatia Zannikou, Stamoulis Stournas and Stamatis Kalligeros. Energies 2 (2009) 362-376.

[5] P. M. Ejikeme, I. D. Anyaogu, C. L. Ejikeme, N. P. Nwafor, C. A. C. Egbuonu, K. Ukogu and J. A. Ibemesi, E-Journal of Chemistry, **7 (**2010) 1120-1132.

[6] Abdelmalik M. Shakorfow and Abdulaziz. H. Mohamed. International Science and Technology Journal, 2020a, Vol.21, 186- 225.

[7] Shakorfow, A. and Mohamed, A. Acta Chemica Malaysia, 2020b, Vol.4 (Issue 2), pp. 76-85.

[8] Shakorfow, A. and Mohamed, Journal of Academic Research (Applied Sciences), 2020c, Vol. 16, pp. 6-11.

[9] Abdelmalik M. Shakorfow and Elham M. Daribi. Acta ChemicaMalaysia, 2022, Vol.6 (Issue 1), pp. 12-19.

[10] Kamaruddin, M. J., N. Mohamad, U. A. Asli, M. A. Ahmad Zaini, K. Kidam, and M. H. Hassim.. Jurnal Teknologi. 2016; vol. 78, no. 8-30

[11] Nomanbhay, Saifuddin, and Mei Yin Ong. Bioengineering (Basel, Switzerland) vol. 4,2 57. 15 Jun. 2017.
[12] Pranjali D. Muley, Yuxin Wang, Jianli Hu and Dushyant Shekhawat. "Microwave-Assisted Heterogenous Catalysis". Specialist Periodical Reports. Catalysis: Volume 33, edited by: James Spivey, Yi- Fan Han and Dushyant Shekhawat. 2021, pp. 1-37.
[13] Kumar R, Sethy AK. Journal of Forest and Environmental Science. 2015;28;31(1):1–6.
[14] Behzad Khedri, Mostafa Mostafaei and Seyed Mohammad Safieddin Ardebili.. 2019; 41:19, 2377-2395,
[15] Moina Athar, Sameer Imdad, Sadaf Zaidi, Mohammad Yusuf, Hesam Kamyab, Jiří Jaromír Klemeš, Shreeshivadasan Chelliapan, Fuel. 2022, Volume 322, 124205.
[16] Yuan-Chung Lin, Kassian T.T. Amesho, Chin-En Chen, Pei-Cheng Cheng, Feng-Chih Chou. Sustainable Chemistry and Pharmacy. 2020, Volume 17,100310.
[17] Barham, J.P., Koyama, E., Norikane, Y., Ohneda, N., Yoshimura, T. Chem. Rec., 2019, 19, 188–203.
[18] Stankiewicz, A., Sarabi, F.E., Baubaid, A., Yan, P., Nigar, H. Chem. Rec. 2019, 19, 40–50.
[19] Surati, Madhvi A., Smita Jauhari and Kishor Ratilal Desai. Archives of Applied Science Research 4, 2012: 645-661.
[20] Sun, J.; Wang, W.; Yue, Q. Materials 2016a, 9, 1-25.
[21]Mohammad Kord; Seyed Mojtaba Sadrameli; Barat Ghobadian. Journal of Renewable Energy and Environment, 3, 4, 2016, 1-9.
[22] Yuan H, Yang B, Zhang H, Zhou X.. International Journal of Chemical Reactor Engineering. 2011;9(1).
[23] Zhang, S.; Zu, Y.-G.; Fu, Y.-J.; Luo, M.; Zhang, D.-Y.; Efferth, T. Bioresource technology vol. 101,3, 2010: 931-6.
[24] Hsiao, M.-C.; Lin, C.-C.; Chang, Y.-H.. Fuel, 2011, 90, 1963–1967.
[25] Patil, P.; Gude, V.G.; Pinappu, S.; Deng, S. Chem. Eng. J. 2011, 168, 1296–1300.
[26] Kumar R, Kumar GR, Chandrashekar N. Bioresour Technol., 2011 Jun;102(11):6617-6620.
[27] H. Venkatesh Kamath, I. Regupathi, M.B. Saidutta.. Fuel Processing Technology, 2011, 92, 100-105.
[28] A.S. Silitonga, A.H. Shamsuddin, T.M.I. Mahlia, Jassinne Milano, F. Kusumo, Joko Siswantoro, S. Dharma, A.H. Sebayang, H.H. Masjuki and Hwai Chyuan Ong. Renewable Energy, 2020, vol. 146, issue C, 1278-1291.
[29] Lin, Jar-Jin, and Yu-Wen Chen. Journal of the Taiwan Institute of Chemical Engineers, vol. 75, June 2017, pp. 43–50.
[30] Venkatesh Kamath, I Regupathi & MB Saidutta. Biofuels, 2010, 1:6, 847-854.
[31] Choedkiatsakul, I.; Ngaosuwan, K.; Assabumrungrat, S.; Mantegna, S.; Cravotto, G. Renew. Energy 2015, 83, 25–29.
[32] Gupta, A.R.; Rathod, V.K. Renew. Energy 2018, 121, 757–767.
[33] Chen, K., Lin, Y., Hsu, K., & Wang, H. Energy 2012, 38, 151-156.
[34] Hsiao, M.C., Kuo, J., Hsieh, S., Hsieh, P., & Hou, S.S. Fuel 2020, 266, 117114.
[35] Hsiao, M.-C.; Liao, P.-H.; Lan, N.V.; Hou, S.-S. Energies 2021, 14, 437.
[36] Fatimah, I.; Rubiyanto, D.; Nugraha, J.. Sustain. Chem. Pharm. 2018, 8, 63–70.
[37] Liao, C.-C.; Chung, T.-W. Chem. Eng. Res. Des. 2013, 91, 2457–2464.
[38] Ye, B.; Qiu, F.; Sun, C.; Li, Y.; Yang, D. Chem. Eng. Technol. 2014, 37, 283–292.
[39] Varol, P.M.; Çakan, A.; Kiren, B.; Ayas, N. Biomass Conv. Bioref., 2021, 1–13.
[40] Wahidin, S.; Idris, A.; Yusof, N.M.; Kamis, N.H.H.; Shaleh, S.R.M. Energy Convers. Manag., 2018, 171, 1397–1404.
[41] Drago, C.; Liotta, L.F.; La Parola, V.; Testa, M.L.; Nicolosi, G. Fuel, 2013, 113, 707–711.
[42] Fatimah, Is, and Septian P. Yudha. Energy Procedia, vol. 105, May 2017, pp. 1796–805.
[43] Sharma, A.; Kodgire, P.; Kachhwaha, S.S. Renew. Sustain. Energy Rev., 2019, 116, 109394.
[44] Majewski, M.W.; Pollack, S.A.; Curtis-Palmer, V.A. Tetrahedron Lett., 2009, 50, 5175–5177.
[45] Perin, G.; Álvaro, G.; Westphal, E.; Viana, L.; Jacob, R.; Lenardão, E.; D'Oca, M. Fuel, 2008, 87, 2838–2841.
[46] Mazzocchia, C.; Modica, G.; Kaddouri, A.; Nannicini, R.. C. R. Chim., 2004, 7, 601–605.
[47] Liu, W.; Yin, P.; Liu, X.; Chen, W.; Chen, H.; Liu, C.; Qu, R.; Xu, Q. Energy Convers. Manag, 76 (2013) 1009–1014.
[48] Lawan, I.; Garba, Z.N.; Zhou, W.; Zhang, M.; Yuan, Z. Renew. Energy, 145 (2020) 2550–2560.
[49] Loy, A.C.M.; Quitain, A.T.; Lam, M.K.; Yusup, S.; Sasaki, M.; Kida, T. Energy Convers. Manag, 180 (2019) 1013–1025.
[50]Jin, Lei, Zhang, Yashan, Dombrowski, James, Chen, Chunhu, Provatas, Anthony, Xu, Linping, Perkins, Christopher, and Suib, Steven. 2011.
[51] Yee, K. F., Lee, K. T., Ceccato, R., Abdullah, A. Z. Bioresource technology, 102 (2011) 4285-9.
[52] Muthu, H., Selvabala, V.S, Varathachary, T. K., Selvaraj, D.K, Nandagopal, J., Subramanian. Brazilian Journal of Chemical Engineering, 27 (2010) 601–8.
[53] Tumba K, Jiyane PC and Musonge P. Front. Energy Res. 9 (2021) 646229.
[54] Shi, W., He, B., Ding, J., Li, J., Yan, F., Liang, X. Bioresource Technology, 101 (2010) 1501–5.
[55] Kulkarni, M. G., Gopinath, R., Meher, L. C., Dalai, A. K. Green Chemistry, 8 (2006) 1056.
[56] Soriano Jr., N.U., Venditti, R., Argyropoulos, D. S. Fuel, 88 (2009) 560–65.
[57]Sutrisno, B., Muhammad, A., Zikriani, G., Hidayat, A. Key Engineering Materials, 872 (2021) 91–95.
[58] Hartono, R., Wijanarko, A., Hermansyah, H. IOP Conf. Series: Materials Science and Engineering, 345 (2018) 012002.
[59] Brito, A., Borges, M., Otero, N. Energy & Fuels, 21 (2007) 3280–83.
[60] Richard N. Gedye, Frank E. Smith, and Kenneth Charles Westaway. (2017) 17-26.
[61] Patil, P.D.; Gude, V.G.; Reddy, H.K.; Muppaneni, T.; Deng, S. Journal of Environmental Protection, 3 (2012) 107–13.
[62] Gude, V.; Patil, P.; Martinez-Guerra, E.; Deng, S.; Nirmalakhandan, N. Sustainable Chemical Processes, 1 (2013) 5.
[63] N. Haneishi , S. Tsubaki , E. Abe , M. M. Maitani , E.-i. Suzuki , S. Fujii , J. Fukushima , H. Takizawa and Y. Wada. Scientific Reports, 9, (2019).
[64] J. Sun, W. Wang, Q. Yue, C. Ma, J. Zhang, X. Zhao and Z. Song. Applied Energy, 175 (2016b) 141–157.
[65]T. Musho, C. Wildfire, N. Houlihan, E. M. Sabolsky and D. Shekhawat, Materials Chemistry and Physics, 216 (2018) 278-284.

Malaysian Journal of Catalysis
http://mjcat.utm.my/
MJCat
Research Article

Microwave-Assisted in the Preparation of Nitrogen-Doped TiO_2 for the Photogradation of Organic Dyes: Effect of pH and Catalyst Dosage

M.S. Azami[a*], K.H. Tan[b], N. Jamaluddin[c], N.M. Izzudin[d], A.A. Azmi[e]

[a]*Faculty of Applied Sciences, Universiti Teknologi MARA, 02600 Shah Arau, Perlis, Malaysia*
[b]*INTI International University, Persiaran Perdana BBN, Putra Nilai, 71800, Nilai, Negeri Sembilan, Malaysia*
[c]*Faculty of Science, Universiti Teknologi Malaysia, 81310 UTM Johor Bahru, Johor, Malaysia*
[d]*School of Chemical and Energy Engineering, Faculty of Engineering, Universiti Teknologi Malaysia, 81310 UTM Johor Bahru, Johor, Malaysia.*
[e]*Graduate School of Science and Engineering, Saga University, 1 Chome Honjomachi, Saga, 840-8502, Jepun*

**Corresponding Author: saifulddinazami@gmail.com*

Article history :
Received 6 April 2022
Accepted 26 June 2022

ABSTRACT

The unmodified TiO_2 was modified using a microwave technique to produce a visible light active nitrogen (N) doped TiO_2. The modified photocatalyst was prepared by mechanical mixing of unmodified TiO_2 with various amounts of urea and various irradiation power of micrcowave . It was observed that the N doped TiO_2 at 800 W of microwave power irradiation with urea content 3 g was defined as the optimum condition for a modified photocatalyst. N doped TiO_2 then was characterized using X-ray photoelectron spectroscopy (XPS), photoluminescence (PL) and UV-Vis diffuse reflectance spectra (UV-Vis/DRS) analyses. The XPS and PL proved that the successful nitrogen doped into the TiO_2. XPS results presented with two peaks with binding energy 404.8 and 400.2 eV that indicates the formation of chemical interaction N with titania forming N doped TiO_2. In addition, UV-Vis/DRS confirmed that the introduction of nitrogen into TiO_2 by decreasing the bandgap energy value from 3.02 eV to 2.9 eV. The photocatalytic activity study of N doped TiO_2 was carried out by irradiating 25 mL of 30, 10 and 5 mg L^{-1} of anionic Reactive Red 4 (RR4), cationic Methyl Violet (MV) and cationic Janus Green dyes (JG) in the presence of fluorescent light and visible light (UV cut-off) with the rate of photodegradation was estimated from aliquot concentration spectrophotometrically. The irradiation of N doped TiO_2 was conducted using two parameters namely the effect of catalyts dosage and the effect of pH. It can be observed that 0.0012 g /mL of catalyst dosages that gives an optimum photocatalytic degradation for both anionic and cationic dyes. Effect of pH was conducted based on the optimum catalyst dosage and conclude that pH 4 and 8 were the optimum pH for anionic and cationic dyes respectively

Keywords: carbon nitride; titanium dioxide; photocatalysis; microwave synthesis.

| eISSN 0128-2581 |

1. INTRODUCTION

In many countries, dyes were mostly consumed in the textile industry. This industry has greatly developed because clothes are a necessity for every human being. However, they generate wastewaters with high chemical complexity, low biodegradability and are highly persistent. This will lead to dramatic environmental contamination, and eutrophication and will cause severe harm to all creatures if there is no immediate action performed. In past decades, a more potent approach for the degradation of dye effluents has received great attention because most of the pollutants were not fully treated under the existing effluent treatment methods [1].

One promising technology is heterogeneous photocatalysis in the presence of semiconductors. This method is one of the advanced oxidation processes (AOPs) and has been widely studied by scientists to overcome this wastewater problem. Decomposition and mineralization of organic contaminants in water by the generation of hydroxyl radicals and super peroxide anion under irradiation was the way this method works [2]. The most widely used photocatalyst was titanium dioxide (TiO_2). This is because it has high photocatalytic activity, strong oxidizing power, is non-toxic, is relatively inexpensive and is also durable [3]. It is also a very well-researched material in photocatalysis due to the stability of its chemical structure, biocompatibility, and physical, optical and electrical properties. Pelaez et al. [1] stated that the TiO_2 has received much attention in the photoinduced process since it is

chemically and biologically inert, relatively easy to produce and use, photo-catalytically stable and able to give efficiency in catalyzing the reaction without risks to the environment or human. However, Nawawi and Nawi [2] stated that TiO_2 have its drawback toward photocatalyst that shows its incapability to absorb visible light. TiO_2 is only active in ultraviolet light due to its large bandgap energy which is 3.2 eV that corresponding to a wavelength shorter than 388 nm. Therefore, TiO_2 could only absorb less than 5% of the solar surface that reaches the earth [3].

To improve the photocatalyst of TiO_2, some modifications have been discovered by shifting its optical response to the visible light regions such as TiO_2 doping with metal and non-metal compounds [4]. The modification of TiO_2 will improve the photocatalyst by narrowing its bandgap allowing the utilization of a wider fraction of the visible light for the production of charge carriers. [5], [6], [7]. Even though its optical response could be shifted to the visible light region, the preparations for samples were complicated. Most current studies stated that the modification of N doped TiO_2 is produce by using the calculations technique. However, the procedure shows deficiency which consumed much energy and took more than 2 hours to prepare modified TiO_2 that can achieve optimum value [2]. In our research, the microwave irradiation technique was successfully applied in the preparation of N doped TiO_2. It was observed that the N doped TiO_2 at 800 W of microwave power irradiation at 3:7 (urea: TiO_2) ratios were defined as the optimum condition for a modified photocatalyst. The N doped TiO_2 could effectively degrade both anionic and cationic dyes under fluorescent light irradiation.

2. EXPERIMENTS

2.1 Preparation of N doped TiO_2

The preparation of N doped TiO_2 was prepared by using the microwave irradiation technique. N doped TiO_2 was prepared by mixing the TiO_2 with various amounts of urea in the mechanical mixing process. The mixed powder was then placed into a conical flask in the semi-closed reactor and heated by using a microwave at various irradiation power. After the irradiation process, the treated sample was cooled to room temperature and named N doped TiO_2.

2.2 Characterization and parameter studies

N doped TiO_2 sample and unmodified TiO_2 photocatalyst were characterized by using UV-Vis diffuse reflectance spectra (UV-Vis/DRS), X-ray photoelectron spectroscopy (XPS) and Photoluminescence (PL) analyses. The photocatalytic activity for photodegradation of RR4, MV and JG dyes was applied to affect the pH of pollutant and catalyst dosage.

2.3 Photocatalysis

For the photocatalytic degradation study, 0.03g of photocatalyst sample was added to the 25ml of 30, 10 and 5 mg L^{-1} of anionic RR4, cationic Methyl Violet and cationic Janus Green dyes respectively to form a suspension. These suspensions were then poured into a custom-made glass cell with dimensions 50mm ×10mm ×80mm (L ×B ×H). The suspension was then irradiated under 55 W fluorescence lamps with UV cut off the filter and the sampling of treated pollutant was collected for every 15 minutes interval until 60 minutes. The treated RR4, Methyl Violet and Janus Green dye every 15 minutes intervals were then collected and filtered using a syringe filter prior measured the absorbance value by using a Spectrophotometer at λ_{max} = 517, 586 and 661 nm for RR4, Methyl Violet and Janus Green respectively.

3. RESULTS AND DISCUSSION

3.1 Optimization studies

The optimum condition for N doped TiO_2 was observed at 800 W in 3 g of urea content with 0.104 min^{-1} of photodegradation rate.

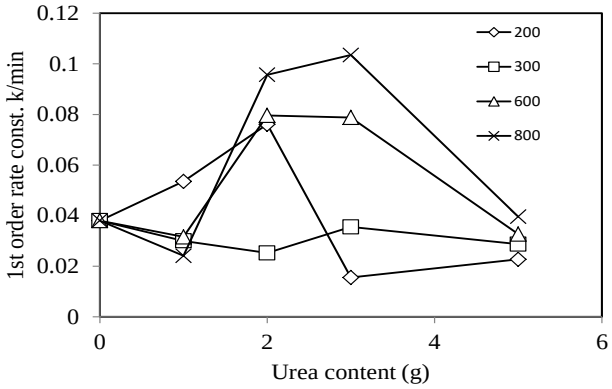

Figure 1**:** Plots of the pseudo-first-order rate constants (K) for the degradation of 30 mg L^{-1} RR4 under 55 W fluorescent lamp for N doped TiO_2 samples prepared at different irradiation power and different amount of urea.

Figure 1 shows a plot degradation rate of RR4 by using a 55-W compact fluorescent lamp on various N doped TiO_2 samples under different microwave irradiation power at 30 minutes. The lower content of urea shows slightly lower in pseudo-first-order rate constants, K values compared to unmodified TiO_2. Increasing the ratio of urea content produced a significant photocatalytic activity where K values were higher as compared with unmodified TiO_2. However, the higher ratio of TiO_2 with urea beyond the optimum sample shows a decrease in K values. The decrease in K value is due to a high amount of N content since the high amount of N may increase the substitution of oxygen

sites by nitrogen. This optimum condition for N doped TiO_2 was conducted in all applications research in this paper.

3.2 Characterization studies

3.2.1 UV-Vis/DRS

Figures 2 (a) and (b) show the UV-Vis diffuse reflectance spectra and plot graph Kubelka-Munk versus energy eV for samples N doped TiO_2 and unmodified TiO_2. Based on Figure 2 a), the absorption edge of unmodified TiO_2 is around 400 nm while for N doped TiO_2 is around 430 nm. A wavelength for UV light is from 200 to 400 nm while the wavelength for visible light is from 401 to 700 nm [8]. At this point, N doped TiO_2 sample shows the shift of its absorption towards the visible light region while the unmodified TiO_2 in the UV region. This observation shows that the N atom in urea was significantly reacted with TiO_2 particles producing a defect structure thus, narrowing the band gap energy of the photocatalyst. Figure 2 (b) shows the graph extrapolate to determine the band gap energy of unmodified and N doped TiO_2. The band gap energy was determined by Tauc's equation.

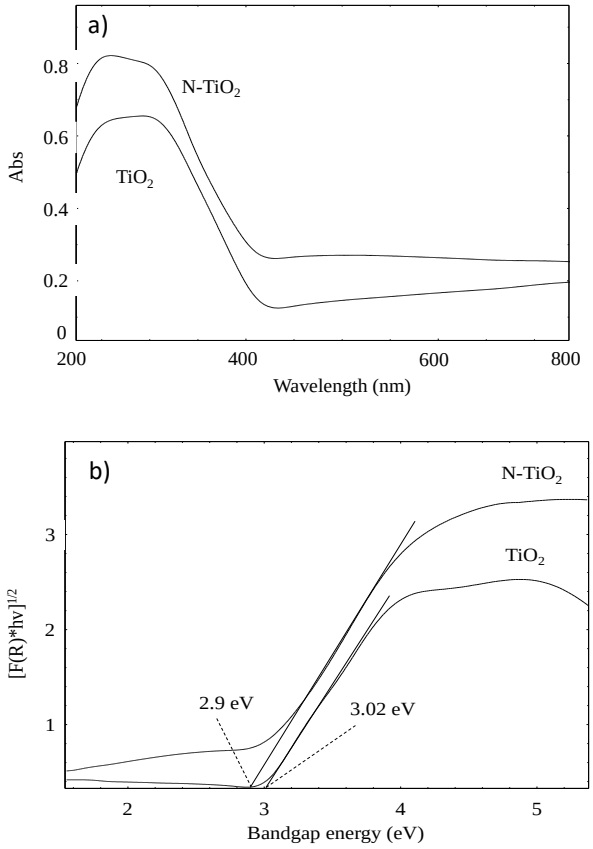

Figure 2: UV-VIS diffuse reflectance spectra of (a) Kubelka-Munk function vs. the energy of the light absorbed and (b) unmodified TiO_2 and N doped P25.

3.2.2 XPS analysis

X-ray photoelectron spectroscopy (XPS) measurement is used to carry out the detection of the surface species on the titania surface responsible for the visible absorption [6]. The N doped TiO_2 shows the presence of N 1s, O 1 s and Ti 2p XPS peaks with binding energy at 404.8, 400.2, 532.16 and 457.96 eV respectively as shown in Figure 3. Based on the previous study, binding energy greater than 400eV indicate there was interstitial N doping and formation of N-O-Ti species.

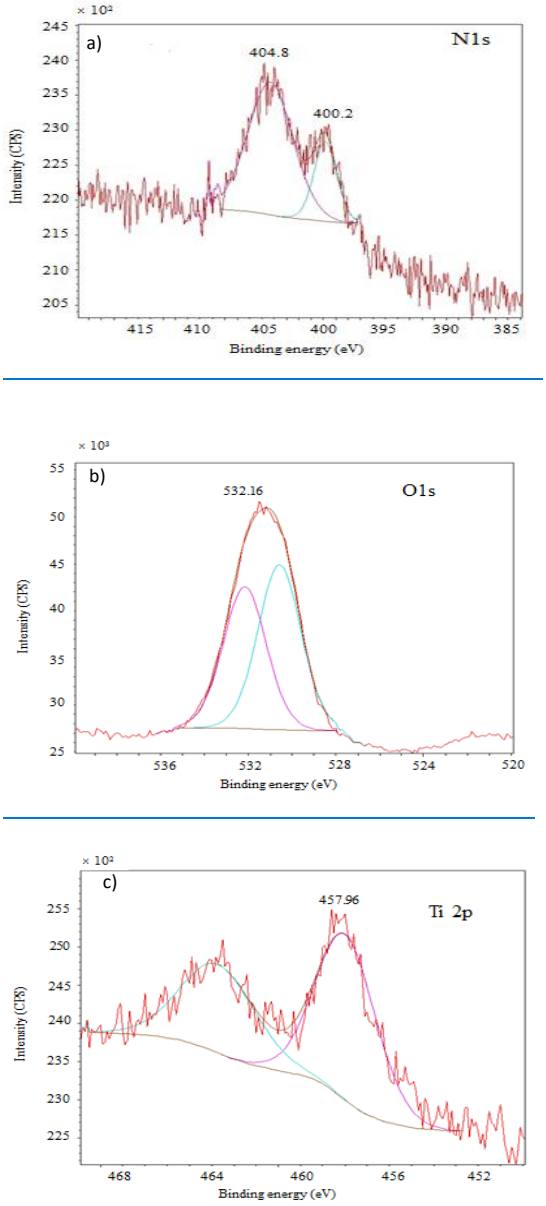

Figure 3: XPS Spectra of N-doped P25. (a) N 1s; (b) O 1s; (c) Ti 2p peaks

Figure 3 a), shows the deconvolution of N 1s peak revealed the presence of two peaks with binding energy 404.8 and 400.2eV in N doped TiO_2 sample. It is shown that a chemical interaction of N with titania forms N doped TiO_2 and this interesting finding explains the sample name (N doped TiO_2). Figure 3 (b) shows the binding energy peak for the O 1s located at 532.16 eV. A previous study by Zhanglian et al. [9] stated that binding energy of about 500 eV was attributed to the presence of metallic oxide, Ti-O. Thus, the binding energy in this study is assigned to the Ti-O structure. Value binding energy is shown in Figure 3 c) indicated to Ti 2p. According to Venkatachalam et al. [10], the Ti 2p region appeared at about 455eV and above. Thus for this sample analysis, it can be deduced that the value 457.96 eV observed in Figure 3 c) assign to the Ti 2p structure.

3.2.3 PL analysis

Photoluminescence (PL) analysis is an optical beam used to excite a material and radiation emitted by the material is spectrally analyzed [11]. PL spectra have been used extensively in the field of photocatalysis to understand the surface process as well as the fate of the electron-hole pairs in TiO_2 particles. Figure 4 shows the PL spectra of pristine TiO_2 and N doped TiO_2 using the excitation wavelength of 325 nm. It can be seen that the peak for both unmodified and N doped TiO_2 shows a similarly shaped curve the peak at about 480 nm and 575 nm. It was generally accepted that nitrogen doping can form a new electronic state (N state) just above the valence band, making TiO_2 absorb visible light. The emission at 480 nm is attributed that the emission signal originating from the charge transfer transition from oxygen vacancy trapped electron[12].

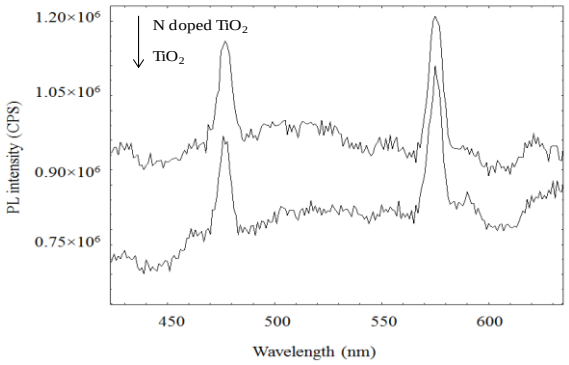

Figure 4: PL analysis of N doped TiO_2

According to Henderson et. al.[13], nitrogen doping favoured the formation of oxygen vacancies, which were experimentally found to be about 0.8 eV below the bottom of the conduction band. The oxygen vacancy of nanosized semiconductors was easily captured or bound with the photo-induced electrons [14]. Hence, the larger the oxygen vacancy content, the stronger the PL intensity. In Figure 4, it can be concluded that oxygen vacancy in N doped TiO_2 sample is in favour of photocatalytic reactions. The larger the content of oxygen vacancy gives the stronger of excitonic PL spectrum and the higher the photocatalytic activity.

3.3 Parameter studies

3.3.1 Effect of catalyst dosage

At the lower catalyst dosage (0.01g), RR4 dye shows around 50% photodegradation while MV and JG show the photodegradation of dyes at around 60% in 1 hour. This is due to the lack of surface-active site to get absorbed and leads to the reduction in the photodegradation rate.

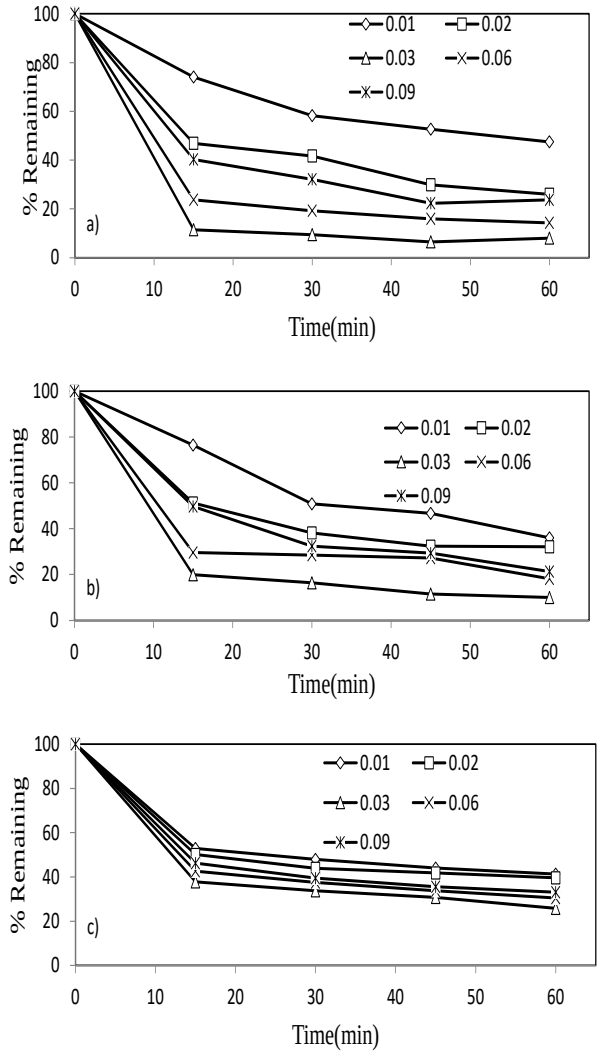

Figure 5: Effect of different catalyst dosage towards photocatalytic degradation based on percent remaining of a) RR4, b) MV and c) JG.

The photodegradation of dyes was gradually increased with optimum dosage achieved at 0.03g whereby RR4, CV and

JG dyes removal were almost 99%. This was due to the increase in the catalyst dosage that lead to the increase in the absorbent surface corresponding to the increasing binding or active site [15]. Thus, more dyes can be removed from the solution due to more molecule dyes can be absorbed onto the adsorbent surface. Therefore, 0.03g is the optimum dosage for N doped TiO_2 sample based on the highest photocatalytic degradation rate under RR4, MV and JG dyes. However, the increment catalyst dosage after the optimum value causes the reduction in the performance of dyes, possibly owing to the excessive particle that can cause turbidity and reduce the light penetration.

3.3.2 Effect of pH

Based on Figure 6 a), N doped TiO_2 shows the value of pH is inversely proportional to the degradation activity of dye. The higher the pH value, the lower the degradation activity of RR4. As we can see in Figure 6 a), the degradation activity of anionic dye is faster in acidic conditions compared to in alkaline conditions. It can be shown by the value of pH is pH 4. This is because the catalyst surface was positively charged and the surface active sites behave as strong Lewis acid [16].

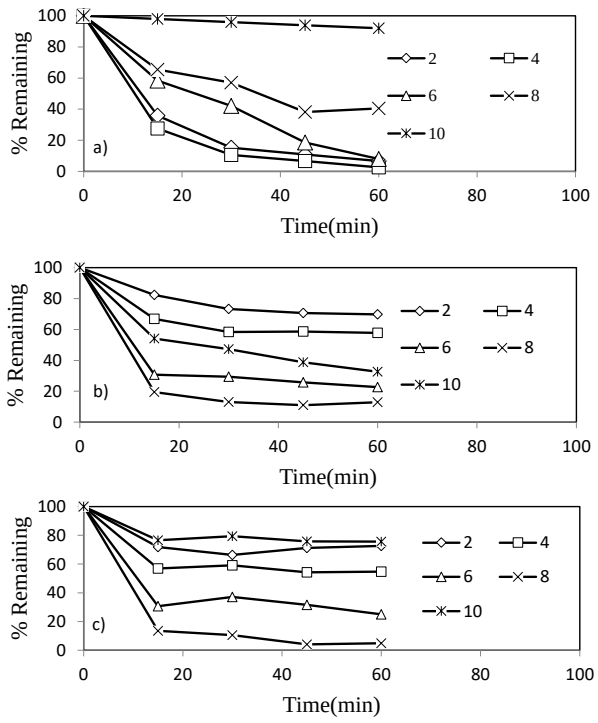

Figure 6: Effect of pH towards per cent remaining of a) Reactive red 4, b) Methyl violet, and c) Janus green dyes

Figures 6 b) and c) illustrates the trend of pH effect on the MV and JG. The MV and JG show the degradation activity was higher in the alkaline condition and lower in the acidic condition. Increasing, pH value indicated the enhancement of absorptivity capacity of cationic dyes, simultaneously faster the degradation activity [12]. MV and JG show the degradation activity highest at pH 8 as shown in Figures 6 b) and c). The MV and JG have higher degradation at pH 8 compared to the ambient pH of 6. This was because there was N doped at the TiO_2 particle. Increasing the pH value from 6 to 8 will increase the negative charge on the surface N doped TiO_2. When the surface is a highly negative charge, MV dye can be easily absorbed and faster degradation [16].

4.0 Conclusion

The microwave irradiation technique was successfully applied in the preparation of N doped TiO_2. It was observed that the N doped TiO_2 at 800 W of microwave power irradiation at 3:7 (urea: TiO_2) ratios were defined as the optimum condition for a modified photocatalyst. N doped TiO_2 was characterized using X-ray photoelectron spectroscopy (XPS), photoluminescence (PL) and UV-Vis diffuse reflectance spectra (UV-Vis/DRS) analyses. The XPS and PL proved the successful nitrogen doped into the TiO_2. In addition, UV-Vis/DRS confirmed the doped of TiO_2 by decreasing the wavelength value. The irradiation of N doped TiO_2 was conducted using two parameters namely the effect of dosage and the effect of pH. It can be observed that 0.03g of catalyst dosage gives optimum photocatalytic degradation. Effect of pH was conducted based on the optimum dosage and conclude that pH 4 and 8 were the optimum pH for anionic and cationic dyes respectively.

REFERENCES

[1] Pelaez M., Nolan N.T., Pillai S.C., Seery M.K., Falaras P., Kontos A.G., Patrick S.M. Dunlop, Jeremy W.J. Hamilton, Anthony Byrne J., Kevin O'Shea, Mohammad H. Entezari, Dionysios D. Dionysiou, A Applied Catalysis B: Environmental, 125(2012) 331– 349.

[2] Nawawi, W.I., Nawi, M.A, Journal of Molecular Catalysis A: Chemical, (2014) 39-45.

[3] Yuan, J., Chen, M., Shi, J., Shangguan., International Journal of Hydrogen Energy, (2006) 1326-1331.

[4] J.F. Zhu, F. Chen, J.L. Zhang, H.J. Chen, M. Anpo, VJ. Photochem. Photobiol. A: Chem.180 (2006) 196–204.

[5] Akpan, U.G., Hameed, B.H, Journal of Hazardous Material. (2009)520-529.

[6] Rengifo-Herrera, J.A., Kiwi, J., Pulgarin, C Journal of Photochemistry and Photobiology A: Chemistry (2009) 109-115.

[7] Barolo, G., Livraghi, S., Chiesa, M., Paganini, M.C., Giamello, E, Journal of Physical Chemistry (2012) 20887-20894.

[8] Orlando C-Neto and Maurício S. B., Cosmeticscope. (2015) 21, 4.

[9] Khalid, N.R., Ahmed, E., Zhanglian, H., Yuewei, Z., Ahmad, M Current Applied Physics (2012)1485-1492.

[10] Venkatachalam N., A. Vinu, Anandan S., Arabindoo B., and Murugesan V., Journal of Nanoscience and Nanotechnology. 6 (2006) 1–9.

[11] Henry M.O., Deicher M., Magerle R., McGlynn E. and Stotzler A., Hyperfine Interactions. 129 (2000) 443–460.

[12] Foo K.Y., Hameed B.H., Chemical Engineering Journal. 173 (2011) 385– 390.

[13] Henderson M. A., Epling W. S., Peden C. H. F., Perkins C. L., Journal Physical Chemistry. B. 107 (2003) 534-545.

[14] Cao Y., Jing L., Shi X., Luan Y., Durrant J. R., Tang J. and Fu H., Physical Chemistry.14 (2006) 8530-8536.

[15] Adam, F., Muniandy, L., Thankappan, R., Journal Colloid Interface Sci., 406 (2013) 209-216.

[16] Gomathi Devi L., Narasimha Murthy B., Girish Kumar S, Chemosphere. 76 (2009) 1163–1166.

Malaysian Journal of Catalysis
http://mjcat.utm.my/
MJCat
Research Article

Fabrication of Zr-Ni Mesostructured Silica Nanocomposites via Consecutive In-Situ Electrolysis for Carbon Dioxide Reforming of Methane

S.M. Sidik[a*], A.A. Jalil[b], N.H.R. Annuar[c], N. Hashim[a], M.S. Rosmi[a]

[a]*Department of Chemistry, Faculty of Science and Mathematics, Universiti Pendidikan Sultan Idris, 35900 Tanjung Malim, Perak, Malaysia*
[b]*School of Chemical and Energy Engineering, Faculty of Engineering, Universiti Teknologi Malaysia, 81310 UTM Johor Bahru, Johor, Malaysia*
[c]*Department of Chemistry, Faculty of Applied Science, Universiti Teknologi Mara (UITM) Johor, Pasir Gudang Campus, 81750 Masai, Johor, Malaysia.*

**Corresponding Author: smunirah@fsmt.upsi.edu.my*

Article history :
Received 17 April 2022
Accepted 20 June 2022

ABSTRACT

Hydrogen production via carbon dioxide reforming of methane (CRM) is a promising technology in solving the environmental problems and global energy. Development of a highly efficient, low-cost and stable catalysts seem to be crucial in accelerating its commercialization. In this study, a bimetallic Zr-Ni catalyst supported on MSN (Zr-Ni/MSN) was successfully prepared via consecutive in-situ electrolysis method. An investigation on the physicochemical properties was conducted using XRD, FESEM-EDX, N_2 adsorption-desorption, and CO_2-TPD analyses. The XRD results prove the successful incorporation of Ni and Zr in the MSN catalysts, and the calculated size of Ni particles were decreased upon the sequential addition of Zr into the catalyst. FESEM and EDX elemental mapping analyses showed that, uniform distribution of spherical MSN particles was distorted to a greater extent upon the addition of Zr in the Zr-Ni/MSN catalyst, due to the formation coral-like mesoporous structure and pyramidal Zr-Ni metal structure. While, N_2 physisorption and CO_2-TPD analyses demonstrated that Zr promoter increased the textural properties and basicity of the catalyst. In the CRM, the Zr-Ni/MSN exhibited highest activity up to 97.6% CH_4 conversion and stability up to 50 h time on stream. The pyramidal structure of Ni-Zr was responsible in promoting better properties in the catalyst, thus led to a higher catalytic activity.
Keywords: nickel; zirconia; mesoporous silica; CO_2 reforming of CH_4; in-situ electrolysis

| eISSN 0128-2581 |

1. INTRODUCTION

The fast depletion of known reserves of fossil fuel is expected to cause energy shortages in the near future [1]. On the other hand, recent studies have been focused on a cleaner and more sustainable ways for energy attaining process to reduce global warming [2]. A dwindling fossil-fuel reserves and worsen climate change phenomena has driven more attention paid to holistic waste management strategies that can utilize waste to produce valuable fuel. Catalytic carbon dioxide reforming of methane (CRM) seems to be a promising route for efficient transformation of two potent greenhouse gases to produce synthesis gas, which can be used as a feedstock for renewable hydrogen or liquid hydrocarbon through the Fischer-Tropsch process [3].

Great efforts have been devoted to develop a suitable catalyst for this reaction. Nowadays, Ni based catalysts have received huge attention and are often chosen as the suitable metal for CRM due to it being more economic and able to produce high catalytic performances [4]. However, Ni-based catalyst deactivated rapidly at high temperature (more than 600 ^oC) owing to the Ni sintering and carbon deposition, which impedes the pace to its commercial utilization [5]. Therefore, considerable efforts have been put on exploring ways to development excellent Ni based with good thermal stability and low coke deposition.

Sidik et al., proved that Ni loaded on mesoporous silica nanoparticles (MSN), Ni/MSN prepared by in-situ electrolysis method significantly affected the catalyst's properties and showed better catalytic performance in DRM compared to the commercially used silica support MCM-41 [6]. The support nature able to assist the gasification of carbon species on the surface of Ni due to the presence of suitable amount of Lewis basicity. In addition, Sidik et al, confirmed that developing bimetallic Ni-Co catalysts is a practical method to boost the activity by increasing the nickel dispersion and minimize metal sintering due to intimate contact between nickel and other metal combined

in the bimetallic system [7]. However, the ability of this catalyst in minimizing coke deposition is still under investigation.

One of the major methods which can reduce coking efficiently is through the addition of promoter on the catalyst. Various metal oxide promoter such as CaO, CeO_2, CuO, La_2O_3, MgO and ZrO_2 able to improve coke-resistant ability of Ni-based catalyst [8]. Among all, ZrO_2 is found to be an outstanding promoter owing to its high thermal stability and strong coke inhibitor properties due to its high oxygen vacancies that promote the carbon removal from metallic Ni surfaces [9]. Abdullah et al, studied different ratio of Zr promoter loaded on Ni/SBA-15 via sol-gel hydrothermal method and found that 1Zr/5Ni/SBA-15 is the optimum catalyst for DRM at 800 ºC with 50 mL/min inlet reactants [10]. Whereas, Okutan et al., investigated a series of Ni-M (M= Al, Ti and Zr) loaded on mesoporous SBA-15 via one-pot hydrothermal method [4].

It is interesting to note that, there is no literature reported on the influence of Zr promoter on structural properties of Ni loaded on MSN prepared via consecutive in-situ electrochemical method for DRM. Thus, in this current study, the influence of Zr promoter loaded on the Ni/MSN via consecutive in-situ electrochemical method toward its physicochemical properties and DRM were investigated.

2. EXPERIMENTS

2.1 Synthesis of mesoporous silica nanoparticles (MSN)

MSN was prepared by co-condensation and sol-gel method as previously reported [11]. In brief, the cetyltrimethylammonium bromide (CTAB, Merck), ethylene glycol (EG, Merck) and ammonium (NH_4OH, QRec) solution were dissolved in 700 mL of double distilled water with the following mole composition of CTAB:EG:NH_4OH:H_2O=0.0032:0.2:0.2:0.1. After vigorous stirring for about 30 min at 50 ºC, 1.2 mmol tetraethylorthosilicate (TEOS, Merck) and 1 mmol 3-aminopropyl triethoxysilane (APTES, Merck) were added to the clear mixture to give a white suspension solution. This solution was then stirred for another 2 h at 80 ºC, and the as-synthesized MSN was collected by centrifugation at 20,000 rpm. The as-synthesized MSN was dried at 110 ºC and calcined at 550 ºC for 3 h to form surfactant-free MSN.

2.2 Preparation of Zr-Ni supported on MSN (Zr-Ni/MSN)

In this study, the Zr-Ni/MSN was prepared by consecutive in-situ electrochemical method, following the procedures reported by [7]. First in-situ electrolysis was conducted to prepare a 2.5wt% Ni/MSN. After calcination at 550 ºC for 3 h, a silver colored Ni/MSN was obtained. Then, a consecutive in-situ electrolysis was carried out to dope the second metal, Zr into the Ni/MSN to give 2.5%Zr-2.5wt%Ni/MSN (Zr-Ni/MSN). As a reference, 5 wt. % of the monometallic Zr/MSN and Ni/MSN were also prepared.

2.3 Characterization

The physicochemical properties of the catalysts were examined by XRD, FESEM-EDX, N_2 physisorption and CO_2-TPD analyses. The XRD was carried out using powder diffractometer (Bruker Advance D8, 40 kV, 40 mA) using a Cu Kα radiation source in the range of 2θ = 1.5-80 º. The crystallite size of NiO (d_{NiO}) was calculated by means of the Scherrer equation. The morphology was observed by FESEM-EDX spectrometer (JSM-6710F). N_2 physisorption isotherms was used to determine the textural properties at liquid nitrogen temperatures using a Beckman Coulter SA 3100 Surface Area Analyzer. CO_2-temperature programmed desorption (CO_2-TPD) analysis was carried out using a flow system equipped with a thermal conductivity detector by Thermo Scientific TPDR1100 flow apparatus. Prior to the experiment, the sample was pretreated at 800 ºC for 1h in 5% H_2/Ar mixture. Subsequently, the sample was treated with He for 2h to remove all chemisorb H_2. Then, it was cooled down to 50 ºC. 10 pulses of CO_2 (99.9 %) were introduced by an electro-actuated valve with a volume of 0.4 mL. The sample was purged with He to remove the weakly absorbed CO_2. Then, the sample was heated again form 50-900 ºC at a heating rate of 10 ºC/min in He flow, the desorbed CO_2 was monitored by a TCD detector.

2.4 Catalytic testing

The catalytic CO_2 reforming of CH_4 was performed in a fixed-bed continuous flow reactor at 400-800 ºC. Prior to the reaction, 0.2 g of the catalyst was treated by H_2 (50 mL min^{-1}) at 850 ºC for 3 h. Then, the reactor was cooling down to a reaction temperature under N_2 stream. CO_2 and CH_4 were mixed at a stoichiometric ratio of 1:1 and N_2 was added as the carrier gas. The reactants with space velocity around 15, 000 mL $g^{-1}h^{-1}$ was passed over the treated catalyst and the products were analyzed using online 6090N Agilent Gas Chromatograph equipped with Carboxen 1010 packed column and TCD detector. The CH_4 conversion was calculated according to the following terms:

$$X_{CH_4} = \frac{[CH_4]_{in} - [CH_4]_{out}}{[CH_4]_{in}} \times 100 \quad (1)$$

where $[CH_4]_{in}$ and $[CH_4]_{out}$ are the molar concentration of CH_4 in the feed and effluent, respectively.

3. RESULTS AND DISCUSSION

Fig. 1 shows the XRD patterns for MSN, ZrO_2, NiO, Ni/MSN, Zr/MSN and Zr-Ni/MSN. Low-angle XRD pattern (Fig. 1A) of MSN, Ni/MSN, Zr/MSN and Zr-Ni/MSN exhibited three distinct peaks at 2θ = 2.35, 4.05 and 4.75 º, which can be assigned to (100), (110), and (200) reflections of a hexagonal mesoporous structure (*p6mm*) of

the MSN [11]. The intensity of these peaks slightly decreased for Ni/MSN and Zr/MSN, indicating a slight distortion of the ordered mesoporous structure after the modification. However, a significant decrease in intensity was observed for Zr-Ni/MSN, demonstrating a greater distortion of the structure. Since the MSN is not crystalline at the atomic and molecule levels, no reflection was observed at higher angles.

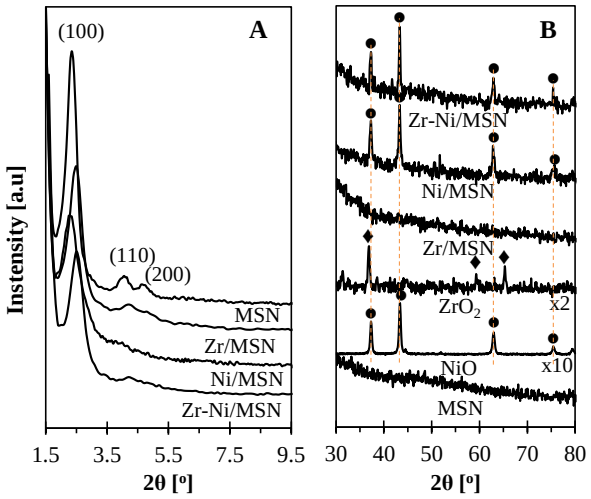

Fig. 1 (A) Low and (B) wide angle of XRD spectra for MSN, Ni/MSN, Zr/MSN, Zr-Ni/MSN, ZrO_2 and NiO. The (●) and (♦) indiciated the presence of NiO and ZrO_2 species, respectively.

As shown in Fig. 1B, the NiO, Ni/MSN and Zr-Ni/MSN exhibited four diffraction peaks at 2θ = 37.3, 43.2, 63.1, and 75.6 º, corresponding to (111), (200), (220), and (311) planes of NiO, respectively (JCPDS 78-0643). The crystal size of NiO in the Ni/MSN and Zr-Ni/MSN calculated using the Scherer equation is 5.62 and 3.21 nm, respectively. The ZrO_2 exhibited three peaks at 2θ = 37.5, 59.4, and 64.6 º, anatase and monoclinic phase of ZrO_2, respectively (JCPDS 42-1467). In the Zr/MSN and Zr-Ni/MSN catalysts, no ZrO_2 characteristic peaks were observed, suggesting that the particles of Zr is highly dispersed on the surface and the size is smaller than the detection limit of XRD device [10]. Eventhough there is no distinguishable peak of Zr was observed in the wide angle Zr-Ni/MSN, an obvious peak shifting was observed in the low angle XRD at 2.35 º. The peak shifting toward higher 2θ for Zr/MSN and Zr-Ni/MSN is probably due to isomorphous substitution caused by the substitution of Si^{4+} ions (0.41 Å) with Zr^{4+} cations (~ 0.84 Å) and structure rearrangement of long-range order of MSN upon the Zr addition [9,12]. The presence of peak shifting also indicating formation of solid solution for supported Ni catalyst [13].

Fig. 2 shows FESEM images of the Ni/MSN and Zr-Ni/MSN at different magnifications. The FESEM image of MSN [11] demonstrated the formation of uniform

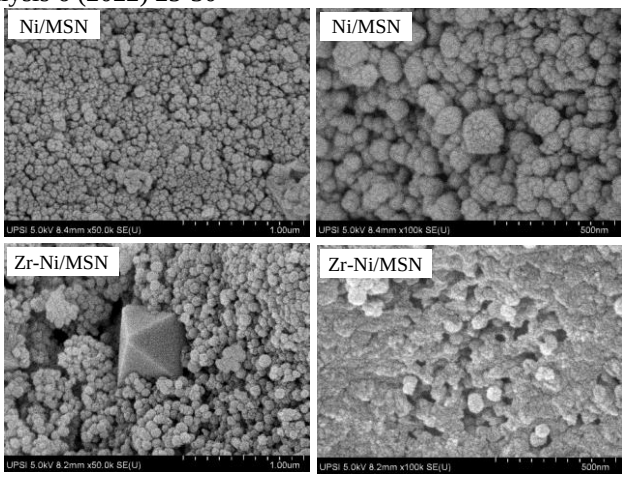

Fig. 2 FESEM images of Ni/MSN and Zr-Ni/MSN at different magnifications.

spherical particles in the size of 40-60 nm. The first in-situ electrolysis process was successful to retain the spherical morphology, but showed an increase in the surface roughness of the catalyst, which is due to the deposition of Ni crystallites [6]. Further addition of Zr in the Ni/MSN catalyst via second in-situ electrolysis process likely seems to disrupt the original MSN's morphology, as the distribution of spherical shape and size is not well uniform, producing a coral-like morphology that have many large holes in between. This may be due to a higher degree of desilication and structural rearrangement of the silica during the consecutive in-situ electrochemical incorporation of the Ni and/or Zr. This observation *agrees* with the XRD results (Fig. 1A), which revealed that incorporation of the Zr and/or Ni led to distortion in the hexagonal silica order.

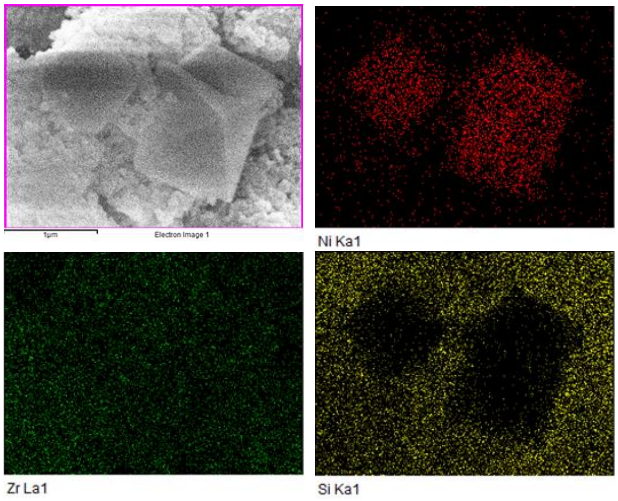

Fig. 3 Elemental mapping analysis of Zr-Ni/MSN.

Interestingly, the Zr-Ni/MSN images showed the existence of new square pyramidal particles. Further EDX-mapping analysis of the pyramidal particles (Fig. 3) elucidated that Zr particles is uniformly distributed on the surface of the catalyst. While Ni particles seemed to dominate the

pyramidal structure area, with the absence of Si particles. This suggested that the Ni and Co particles are located closed to each other at the area of pyramidal structure and possibly might formed an interaction [14].

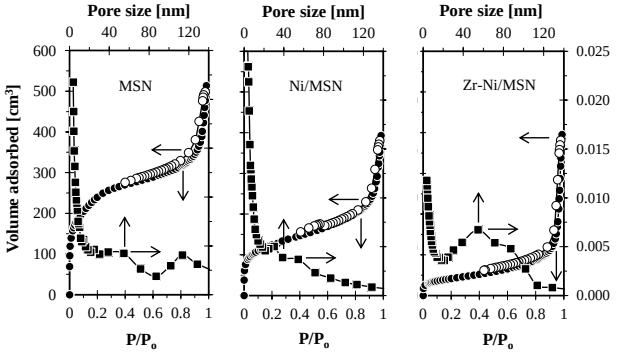

Fig. 4 N_2 adsorption-desorption isotherms and pore size distribution curves for MSN, Ni/MSN and Zr-Ni/MSN.

The textural properties of the MSN, Ni/MSN and Zr-Ni/MSN were determined by N_2 adsorption-desorption analysis. The N_2 adsorption-desorption isotherms and pore size distributions of the catalysts are illustrated in Fig. 4. According to the IUPAC classification, the isotherm of the catalysts exhibited typical Type IV adsorption steps at P/P_o = 0-0.1, 0.3-0.4, and 0.9-1.0, which could be classified as a mesoporous material [15]. Although the adsorption steps clearly remained for Ni/MSN and Zr-Ni/MSN, these catalysts showed a remarkable decrease in N_2 adsorption and pore volume compared to the MSN. This indicated that the rearrangement of silica order and pore fillings were occurred during the metal incorporation [16]. In the pore size distributions, all the catalysts demonstrated a bimodal pore structure in the range of 0-20 nm and 20-80 nm. Compared to the MSN, the intensity of pore distribution in both ranges decreased with the addition of Ni or/and Zr. This observation is correlated with the reduction in the quantity of adsorbed N_2 in Ni/MSN at P/P_o = 0-0.05 and 0.9-1.0, which indicates the reduction of micropores and interparticles void mesopores due to the pore blockage by metal. As for Zr-Ni/MSN, the reduction of micropores in the range of 0-20 nm is even greater which probably caused by a greater pore blockage. Besides, increment of larger pore in the range 20-80 nm was observed, probably due to the increase number of interparticles voids resulted from the new coral-like structure of the MSN (as been shown in Fig.2). In this study, MSN showed the highest surface area and pore volume about 894 m^2g^{-1} and 0.979 cm^3g^{-1}, respectively. The addition of Ni or/and Zr to the MSN resulted in reduction of the surface area and pore volume to 442 and 622 m^2g^{-1}, and 0.585 and 0.799 cm^3g^{-1}, respectively. A decrease in surface area and pore volume with the addition of Ni was attributed to partial pore blockage and/or pore filling of the catalysts [17]. In contradiction, consecutive addition of Zr enhanced the texture properties of the catalyst, which can be attributed to increased interparticles voids. This finding is in accordance to the morphology study that found that coral-like morphology that have many large holes in between.

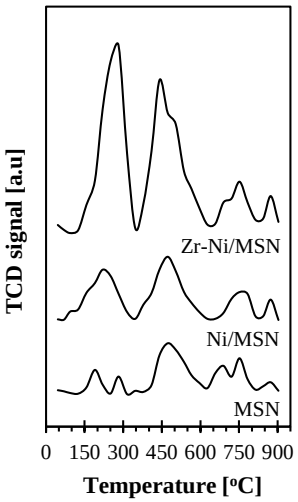

Fig. 5 CO_2-TPD profiles of MSN, Ni/MSN and Zr-Ni/MSN.

To assess the surface basicity of the catalysts, CO_2-TPD analysis were carried out. As shown in Fig. 5, CO_2 was released in two main temperature range reflecting different type of carbonate-like species chemisorb on the surface of the catalyst. In agreement with literature [18], bridged (α species) and bidentate (β species) carbonates desorbed as CO_2 at temperature lower than 250 ºC, whereas carboxylate and monodentate carbonates (γ species) desorbed at higher temperature. TPD profile of MSN showed 6 small desorption peaks at 190, 282, 473, 689, 752 and 873 ºC. The Ni/MSN showed a greater number of basic sites compared to MSN, distributed in desorption peaks at 251, 504, 783 and 873 ºC. While for Zr-Ni/MSN, the highest number of basic sites can be observed from the very sharp peak at 282, 441, 752 and 873 ºC. From the analysis, we can see that addition of Ni was successful to improve the mild basic sites, which being assigned around 150-300 ºC. Whereas for Zr, it is clearly observed that it can provide large number of mild and strong (more than 400 ºC) basic sites to the catalyst. Therefore, the surface basicity of the catalyst can be arranged in the following order: Zr-Ni/MSN > Ni/MSN > MSN. A higher number of basic sites is beneficial to enhance CO_2 adsorption and dissociation.

The initial activity of the catalysts in CRM was studied at different temperature ranging from 400 – 800 ºC. A comparative test over MSN is inactive and showed less than 5 % CH_4 conversion even at the highest temperature studied. The activity Ni/MSN and Zr-Ni/MSN are shown in Table 1. As it can be seen, these Ni/MSN and Zr-Ni/MSN demonstrated an increasing trend of CH_4 conversion with increasing temperature and significant activity in the 500-800 ºC, as in accordance with the thermodynamic studies of CRM. It is noteworthy that the Zr-Ni/MSN catalysts presented higher conversion than Ni/MSN, suggesting that the smaller Ni particles in Zr-Ni/MSN catalysts could activate more reactants conversion. Moreover, a larger pore

volume and surface area could provide higher accessible site between the active metal and reactants. It is widely accepted that the CH_4 decompositionon the catalyst's active sites is the rate limiting step of the overall process in CRM. Since CH_4 decomposition is a structure-sensitivity reaction, the particle size of the metal has been considered as the key factor to enhance the activity [19]. From the XRD analyses, it was demonstrated that the Ni particle size in Zr-Ni/MSN was slightly reduced and the Ni dispersion was improved with respect to the Ni/MSN. In fact, the small metal particle and better metal dispersion will contribute to more edges and more metal-support structures, and leading to more active sites.

Besides, in the 700 to 800 °C temperature interval, the CH_4 conversion of Zr-Ni/MSN kept higher than the thermodynamic limit values calculated from a direct minimization of Gibbs free energy method using Aspen Plus software [19] and equilibrium data calculated in minimized carbon process condition using DETCHEM software [17]. This result suggest a more intense CH_4 cracking process when CRM is conducted using the Zr-Ni/MSN catalyst under the studied reaction parameters. Stability of Ni/MSN and Zr-Ni/MSN was also tested for 50 h time on stream at 800 °C. Fig. 6 shows the reactants conversion profiles versus time selected.

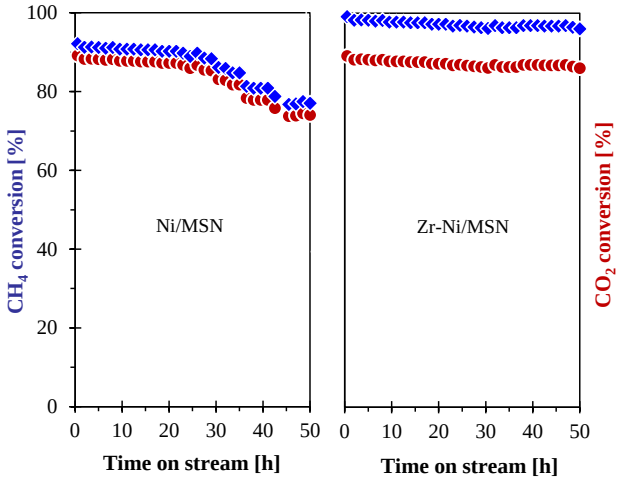

Fig. 6 Evolution of CH_4 and CO_2 conversions with time on stream for Ni/MSN and Zr-Ni/MSN catalysts at 800 °C.

Both Ni/MSN and Zr-Ni/MSN showed a stable CH_4 conversion in 30 h time on stream, but the activity of Ni/MSN started to decrease monotonically earlier compared to Zr-Ni/MSN. This may due to the homogeneous distribution of Zr on the surface of the catalyst, which is beneficial in preventing the generation of carbon on the Ni surface. This phenomenon promoted a higher CO_2 adsorption and facilitated a greater CO_2 activation, which resulted in the enhancement of carbon elimination by the reaction of oxygen with carbon intermediate to yield CO [20]. Thus, a lower coke deposit was formed on the catalyst surface and the stability of the catalyst was sustained. As reported by the previous study, the Ni-based catalyst is prone to metal deactivation by sintering and carbon formation [5]. However, in this case, the incorporation of Zr as the promoter in the Zr-Ni/MSN had boosted the activity for a longer period and suppress the carbon formation. From the characterization and catalytic activity results, it can be inferred that synergism occurred between Ni and Zr, where these elements have a mutual role to improve the CRM activity. The interaction formed between Ni and Zr in the pyramidal structure not only able to confine the Ni agglomeration, but also increase the number of Ni-Zr boundaries which could promote oxidation of carbon species formed from the CH_4 dissociation on the Ni metal sites. An illustration of the relationship between particles metal particle size and basicity of Ni-Zr/MSN toward carbon removal inspired by conceptual model established by Huang *et al.,* 2011 [21] and Theofanidis *et al*., 2016 [22] is depicted in Fig. 7.

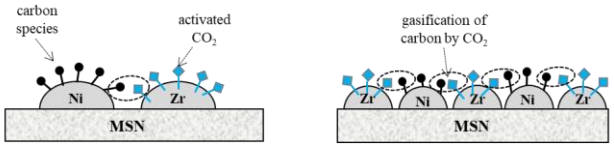

Fig. 7 Conceptual illustration on the relationship of particle size and basicity towards carbon removal.

On a larger metal particle, the carbon species far away from the periphery of the metals tend to nucleate since they cannot reach the activated CO_2. With the increase in time on stream, carbon deposition accumulates in the large particles and cover the metal surface, which results in activity loss [23]. While, for a smaller metal particles, the carbon species derived from the dissociate adsorption of CH_4 near the periphery of the metal particles is easy to react with the activated CO_2 to form CO. While, an increase of basic sites promoted by Zr species enhances the ability of catalyst to adsorb CO_2 in the CO_2 reforming of CH_4. Then, the more adsorbed CO_2 reacts quickly with C species on the Ni surface to form CO. Increased number of Ni-Zr boundaries helps to reduce mass-transfer rate of CO_2 to react with C, and carbon gasification process could proceed as soon as possible, thus reducing coke formation.

Table 1 CH_4 and CO_2 conversion for CRM reaction at different temperatures.

Temperature (°C)	CH_4 conversion			CO_2 conversion		
	This study	Equilibrium[c]	Equilibrium[d]	This study	Equilibrium[c]	Equilibrium[d]
500	17.9[a], 27.3[b]	-	-	12.3[a], 23.3[b]	-	-
600	53.6[a], 63.5[b]	-	-	41.6[a], 58.1[b]	-	-
700	77.2[a], 93.4[b]	92	84	74.5[a], 86.4[b]	65	91
800	94.3[a], 97.6[b]	96	95	91.7, 93.7[b]	88	97

[a]Experimental data obtained in this study for Ni/MSN catalyst
[b]Experimental data obtained in this study for Zr-Ni/MSN catalyst
[c]Data reported in [19] based on direct minimization of Gibbs free energy method using Aspen plus software.
[d]Data reported in [17] based on DETCHEM software in minimized carbon formation processess conditions.

4. CONCLUSION

In this study, Zr-Ni/MSN was successfully prepared by a consecutive in-situ electrolysis. XRD analyses demonstrated that the Zr-Ni/MSN has smaller and better dispersion of metal particles with respect to the Ni/MSN. The addition of Zr as the promoter in Zr-Ni/MSN favored the formation of coral-like mesoporous structure nanoparticles and enhance the surface area of the catalyst, as proven by FESEM and N_2 physisorption analyses. EDX elemental mapping suggested that the pyramidal structure is consisted of homogenous dispersion of Zr and Ni, with higher density of Ni particles. The Zr-Ni/MSN catalyst demonstrated excellent performance for CO_2 reforming of CH_4. The synergy effect between Ni and Zr in the catalyst not only provided high activity, but also a better carbon tolerant ability, with a stable performance for more than 30 h time on stream. Lastly, those square pyramidal structures of Ni-Zr could act as a one stop center to the catalyst as it could react in bi-functional mechanism: i) CH_4 dissociation on the Ni metal sites, and ii) CO_2 adsorption and activation by Zr species. It is believed that this work is a great contribution to the development of nano-catalyst for energy production, particularly towards the utilization of harmful greenhouse gases into valuable syngas.

ACKNOWLEDGEMENTS

This work is supported by the Universiti Pendidikan Sultan Idris and Universiti Teknologi Malaysia through Research University Grant no.0147-101-01 and 05H09, respectively. Our gratitude also goes to the Hitachi Scholarship Foundation for the Gas Chromatograph Instrument Grant.

REFERENCES

[1] D.C. Wilson, Waste Management Research 25 (2007) 198.
[2] R. G. dos Santos, A.C. Alencar. International Journal of Hydrogen Energy 45 (2020) 18114.
[3] V. Wells, A. Riaz, Q. Sun, X. Li, N. Yan, C.-H. Wang, W. Lipinski, Applied Physical Letters 120 (2022) 143905.
[4] C. Okutan, H. Arbag, N. Yasyerli, S. Yasterli. International Journal of Hydrogen Energy 45 (2020) 13911.
[5] A.H. Fakeeha, A.S. Al-Fatesh, A.A. Ibrahim, A.E. Abasaeed. Journal of Saudi Chemical Society 25 (2021) 101244.
[6] S.M. Sidik, A.A. Jalil, S. Triwahyono, T.A.T. Abdullah, A. Ripin. RSC Advances 5 (2015) 37405.
[7] S.M. Sidik, S. Triwahyono, A.A. Jalil, Z.A. Majid, N. Salamun, N.B. Talib, T.A.T Abdullah, Chemical Engineering Journal 295 (2016) 1.
[8] Y. Wang, L. Yao, Y. Wang, S. Wang, Q. Zhao, D. Mao, C. Hu. ACS Catalysis 8 (2018) 6495.
[9] M. Prasad, K. Ray, A. Sinhamahapatra, S. Sengupta. Journal of Material Sciences 57 (2022) 2839.
[10] N. Abdullah, N. Ainirazali, H. Ellapan. International Journal of Hydrogen Energy 48 (2021) 24806.
[11] A.H. Karim, A.A. Jalil, S. Triwahyono, S.M. Sidik, N.H.N. Kamarudin, R. Jusoh, N.W.C. Jusoh, B.H. Hameed. Journal of Colloid and Interface Sciences 386 (2012) 307.
[12] M.S. Aw, I.G.O. Črnivec, P. Djinović, A. Pintar. International Journal of Hydrogen Energy 24 (2014) 12636.
[13] L. Pastor-Pěrez, E. Le Sache, C. Jones, S. Gu, H. Arellano-Garcia, T.R. Riena. Catalysis Today. 317 (2018) 108.
[14] L. Xu, X. Wen, M. Chen, C. Lv, Y. Cui, X. Wu, C. Wu, B. Yang, Z. Miao, X. Hu. Fuel 282 (2020) 118813.
[15] P. Hongmanorom, J. Ashok, S. Das, N. Dewangan, Z. Bian, G. Mitchell, S. Xi, A. Borgna, S. Kawi. Journal of Catalysis 387 (2020) 47.
[16] L. Lyu, M. Shengene, Q. Ma, J. Sun, X. Gao, H. Fan, J. Zhang, T.-S. Zhao. Fuel 310 (2022) 122375.
[17] F. Agueniou, H. Vidal, M.P. Yeste, J.C. Hernández-Garrido, M.A. Cauqui, J.M. Rodríquez-Izquierdo, J.J. Calvino, J.M. Gatica. Catalysis Today 383 (2022) 226.
[18] I. Luisetto, S. Tuti, C. Romano, M. Boaro, E.D. Bartolomeo, J. K. Kasavan, S.M.S. Kumar, K. Selvakumar. Journal of CO_2 Utilization 30 (2019) 63.
[19] M.K. Nikoo, N.A.S. Amin, Fuel Processing Technology 92 (2011) 678.
[20] S.S. Miri, F. Meshkani, A. Rastegarpanah, M. Rezaie. Chemical Engineering Science 250 (2022) 116956.
[21] T. Huang, W. Huang, J. Huang, P. Ji. Fuel Processing Technology 92 (2011) 1868.
[22] S.A. Theofanidis, R. Batchu, V.V. Galvita, H. Poelman, G.B. Marin. Applied Catalysis B: Environmental 185 (2016) 42.
[23] Y. Wang, Z. Zhang, S. Zhang, Y. Wang, S. Hu, J. Ziang, T. Wei, S. Niu, X. Hu. Journal of the Energy Institute 101 (2022) 277.